Alzheimer's Research & Therapy

RESEARCH

Open Access

Deletion of *Abi3/Gngt2* influences age-progressive amyloid β and tau pathologies in distinctive ways

Kristen R. Ibanez[1], Karen N. McFarland[1,2], Jennifer Phillips[1], Mariet Allen[3], Christian B. Lessard[1], Lillian Zobel[1], Elsa Gonzalez De La Cruz[1], Shivani Shah[1], Quan Vo[1], Xue Wang[4], Zachary Quicksall[4], Daniel Ryu[1], Cory Funk[5], Nilüfer Ertekin-Taner[3,6], Stefan Prokop[1,7,8], Todd E. Golde[1,8,9] and Paramita Chakrabarty[1,8,9*]

Abstract

Background: The S209F variant of Abelson Interactor Protein 3 (*ABI3*) increases risk for Alzheimer's disease (AD), but little is known about its function in relation to AD pathogenesis.

Methods: Here, we use a mouse model that is deficient in *Abi3* locus to study how the loss of function of *Abi3* impacts two cardinal neuropathological hallmarks of AD—amyloid β plaques and tau pathology. Our study employs extensive neuropathological and transcriptomic characterization using transgenic mouse models and adeno-associated virus-mediated gene targeting strategies.

Results: Analysis of bulk RNAseq data confirmed age-progressive increase in Abi3 levels in rodent models of AD-type amyloidosis and upregulation in AD patients relative to healthy controls. Using RNAscope in situ hybridization, we localized the cellular distribution of Abi3 in mouse and human brains, finding that Abi3 is expressed in both microglial and non-microglial cells. Next, we evaluated *Abi3*$^{-/-}$ mice and document that both *Abi3* and its overlapping gene, *Gngt2*, are disrupted in these mice. Using multiple transcriptomic datasets, we show that expression of *Abi3* and *Gngt2* are tightly correlated in rodent models of AD and human brains, suggesting a tight co-expression relationship. RNAseq of the *Abi3-Gngt2*$^{-/-}$ mice revealed upregulation of *Trem2*, *Plcg2*, and *Tyrobp*, concomitant with induction of an AD-associated neurodegenerative signature, even in the absence of AD-typical neuropathology. In *APP* mice, loss of *Abi3-Gngt2* resulted in a gene dose- and age-dependent reduction in Aβ deposition. Additionally, in *Abi3-Gngt2*$^{-/-}$ mice, expression of a pro-aggregant form of human tau exacerbated tauopathy and astrocytosis. Further, using in vitro culture assays, we show that the AD-associated S209F mutation alters the extent of ABI3 phosphorylation.

Conclusions: These data provide an important experimental framework for understanding the role of *Abi3-Gngt2* function and early inflammatory gliosis in AD. Our studies also demonstrate that inflammatory gliosis could have opposing effects on amyloid and tau pathology, highlighting the unpredictability of targeting immune pathways in AD.

Keywords: Alzheimer's disease, Plaque burden, Neurofibrillary tangle, Disease signature, Risk factor, Gene dose

Background

Alzheimer's disease (AD) is associated with several canonical pathological hallmarks such as extracellular amyloid β (Aβ) deposits, intracellular neurofibrillary tangles (NFT) of tau protein and robust immune activation

*Correspondence: pchakrabarty@ufl.edu

[1] Center for Translational Research in Neurodegenerative Disease, University of Florida, 1275 Center Drive, Gainesville, FL 32610, USA
Full list of author information is available at the end of the article

[1]. Activation of innate immunity is an integral part of the AD pathological cascade, though its role is not fully understood due to the diversity and complexity of the immune signaling processes [2, 3].

Recent genetic and transcriptomic data have highlighted the involvement of immune signaling processes in AD pathogenesis [4]. Several genes, whose expression is thought to be enriched in microglial cells, have been implicated as AD risk factors [5]. One of these recently identified genes encodes the Abl Interactor family member 3 (ABI3), also known as NESH (new molecule including SH3) [6, 7]. The S209F *ABI3* variant (rs616338:p.Ser209Phe) increased the risk of AD (OR = 1.43, $p = 4.5 \times 10^{-10}$, MAF = 0.008) [6, 7] and has been validated in a secondary study [8].

The ABI3 protein contains a Src homology 3 (SH3) domain, a homeobox homology domain, and several proline-rich and serine-rich motifs [9]. Its putative function, largely based on analogy to function of other family members, is to regulate actin polymerization resulting in reduced ectopic metastasis of tumor cells and cell migration [10]. In the periphery, it is highly expressed in spleen, lymph node, and appendix. In the brain, its expression has been reported to be enriched in microglia with ramified or amoeboid morphology [11]. Single-cell data from mouse brain suggests low level expression in microglia ([12]; data available from: celltypes.brain-map.org). In the brain, it may also play a role in dendritic spine morphogenesis [13]. Though the function of ABI3 in Alzheimer's pathogenesis or any neurodegenerative disease is unknown, co-expression network analysis suggests a close functional relationship with at least two other AD-related microglial genes, *TREM2* and *SPI1* [6].

Here we have evaluated expression of Abi3 in mouse models of AD and in bulk RNAseq studies of human brain. RNAseq data revealed that Abi3 mRNA levels consistently increased in human AD and *APP* transgenic mouse model, but not in a *MAPT* transgenic model. We localized Abi3 RNA in both microglia and in non-microglial cells in human AD and an *APP* transgenic mouse model using in situ hybridization methods. We then characterized an *Abi3*$^{-/-}$ mouse line (B6N(Cg)-Abi3tm1.1(KOMP)Vlcg/J), and the effects of loss of *Abi3* locus on amyloid and tau pathologies. Initial characterization using bulk RNAseq of the brain reveals loss of expression of an overlapping gene, *Gngt2*, indicating these mice are better referred to as *Abi3-Gngt2*$^{-/-}$. Notably, these mice showed early upregulation of an immune gene expression profile, characterized by increased levels of Trem2, Plcg2, and Tyrobp, that has been previously documented to be induced in rodent models of AD pathologies and in AD brains. Haploinsufficiency (+/−) or complete knockout (−/−) of the *Abi3-Gngt2* reduced Aβ levels in an *APP* mouse model. This beneficial effect was diminished as the mice aged. In *Abi3-Gngt2*$^{-/-}$ mice, overexpression of a pro-aggregant tau using neonatal delivery of adeno-associated viruses (AAV) resulted in increased tau pathology and astrocytosis. We further find that the S209F ABI3 variant alters phosphorylation of ABI3, providing initial insight into how this mutant may modulate ABI3 function. These data highlight the complex modality of relationship between immune function and AD relevant pathologies [2], and reinforce the notion that factors that alter immune signaling often have opposing effects on amyloid and tau.

Methods

Mice

All animal studies were approved by the University of Florida IACUC and recombinant DNA use was approved by University of Florida EH&S Office. In this study, we have created several lines of new transgenic *APP* mouse models that are deficient in *Abi3*. We obtained live *Abi3*$^{+/-}$ mice on a BL/6 background from Jax Labs (B6N(Cg)-Abi3tm1.1(KOMP)Vlcg/J; Stock #028180). *Abi3*$^{+/-}$ mice were bred to TgCRND8 mice (*APP*swe/ind) [14], maintained on BL/6xC3H background, which were then crossed with *Abi3*$^{-/-}$ mice to generate the three different *Abi3* genotypes (wild type, WT:+/+; heterozygous, Het:+/−; knockout, KO: −/−) with or without the *APP* transgene. Mice were healthy and without any obvious phenotype, except sudden death of 25% of *APP* transgenic mice (as observed in parental TgCRND8 mice). Mice were maintained on food and water ad libitum on a 12-h light/dark cycle. All animals were euthanized following IACUC-approved procedures, with AAV expressing animals additionally being perfused intracardially post mortem with cold saline. Brains were collected immediately, with left hemisphere flash frozen and right hemisphere drop-fixed in 10% normal buffered formalin. The sex distribution of each cohort is indicated in the figures (open or closed circles) or indicated in figure legends.

Human tissue specimens

Formalin-fixed, paraffin-embedded brain tissue samples of de-identified patients with AD and normal control subjects were provided by the University of Florida Neuromedicine Human Brain and Tissue Bank (UF HBTB) following institutional regulations.

AAV production and neonatal injection

Recombinant AAV was produced and injected in neonatal mice on day P0 as described earlier [15]. Specifically, an AAV construct expressing the 0N/4R human tau construct under the control of CBA promoter [16]

was packaged in capsid serotype 1 for these experiments. Control mice were injected with an empty vector (AAV vector backbone, CTR0, packaged in serotype 1). All animals were injected with 2 µl (2×10^{10} vector genomes) of AAV1 in the cerebral ventricles of each hemisphere as described before [15].

Biochemical extraction of proteins from brain

Frozen hemibrains (forebrain, without cerebellum or olfactory bulbs) were cryopulverized and split into two groups for *APP* mice, one for biochemical analysis and another for RNA analysis. All ultracentrifugation was done in a Beckman Optima TLX centrifuge with a fixed angle TLA55 rotor. All lysates were prepared to a final concentration of 1 ml/150 mg of dry tissue. The first aliquot was weighed on dry ice and added to RIPA buffer (50 mM Tris–HCl, 150 mM NaCl, 1% Triton X-100, 0.5% deoxycholate, 0.1%SDS, 1 × protease/phosphatase inhibitor cocktail). Tissues were homogenized using Tissue Master (Omni International Tissue Master 125) for 30 s. Tissue homogenate were centrifuged at 43,000 rpm for 1 h at 4 °C. Supernatant was aliquoted and stored at − 80 °C as the RIPA lysate. The residual pellet was resuspended in 2% sodium dodecyl sulfate (SDS), sonicated with 3 bursts of 1 min each (Misonix Q700), and then centrifuged at 43,000 rpm for 1 h at 15 °C. The supernatant was aliquoted and stored at − 80 °C as the SDS lysate. The pellet was resuspended in 70% formic acid (FA), sonicated, centrifuged at 43,000 rpm at 15 °C, and the supernatant stored at − 80 °C as the FA lysate.

For AAV-injected brain, the brains were cryopulverized and extracted using tau-specific buffer conditions as described before [16]. Briefly, brains were homogenized (Omni International) in appropriate amount of TBS buffer (50 mM Tris base, 274 mM NaCl, 5 mM KCl, pH 8) containing protease and phosphatase inhibitors (Pierce Protease & Phosphatase Inhibitor Mini Tablets, Thermo Scientific). Following centrifugation at 22,000 rpm for 20 min at 4 °C in a Beckman ultracentrifuge, supernatant was stored at − 80 °C as S1. The pellet, P1, was resuspended in high salt buffer (10 mM Tris base, 0.8 M NaCl, and 10% sucrose) containing 0.05% Triton x-100 (Fisher) and protease and phosphatase inhibitors (Pierce Protease & Phosphatase Inhibitor Mini Tablets, Thermo Scientific) and separated at 22,000 rpm for 20 min at 4 °C into S2 and P2. Pellet P2 was resuspended in 1% sarkosyl, incubated at 37 °C for 1 h with intermittent gentle shaking and separated at 60,000 rpm for 1 h at 15 °C into S3 and P3. Pellet P3 was resuspended in urea/SDS buffer (4 M urea, 2% SDS, and 25 mM Tris–HCl, pH 7.61) by sonicating (Misonix sonicator) and separated at 50,000 rpm at 15 °C for 30 min. The resulting supernatant S4 was designated as insoluble NFT tau.

Immunohistochemical and histological analysis

Formalin-fixed paraffin-embedded brain sections were deparaffinized using standard procedure (described in [16]) and antigen retrieval performed with steam. Slides were blocked in 2% FBS in 1 × PBS for 1 h at room temperature followed by primary antibody incubation at 4 °C overnight (Additional File 1: Table S1). Appropriate secondary antibody (ImmPress reagents, Vector Labs) was used followed by detection using DAB (Vector Labs) and hematoxylin counterstaining. Slides were mounted in Permount mounting media. ThioS staining was done by incubating deparaffinized and rehydrated slides in 1% ThioS (Additional File 1: Table S1) for 7 min at room temperature. Slides were quickly washed in 70% ethanol and then water and mounted with Fluoromount containing DAPI.

Analysis of immunochemical and histological images

Images of stained slides were captured using Scanscope XT image scanner (Aperio, Vista, CA, USA) and percent area of immunostained slides was quantified with the Positive Pixel Count program (Aperio) that detects DAB staining. Three sections per brain was selected and quantified. Data is presented as % immunoreactivity ± SEM and statistical comparisons were conducted using 1-way ANOVA with a Tukey post hoc test, if necessary. Fluorescent images were captured using BZ-X710 All-in-one fluorescence microscope (Keyence Co., Itasca, IL). MC1-stained sections and ThioS-stained sections were manually counted for the number of cells or plaques (respectively) positive for the stain.

Biochemical analysis of tissue lysates

Protein concentrations of RIPA and SDS fractions (in *APP* mice) and S4 fractions (in AAV-tau expressing mice) were determined using Bicinchoninic Acid assay (Pierce BCA Protein Assay Kit, Thermo Scientific). Twenty to twenty-five micrograms of RIPA or SDS lysate or 1 µg of S4 lysate was separated in a 4–20% Tris–glycine gel (Novex, Invitrogen) and transferred to PVDF membranes. Membranes were blocked for 1 h in 0.5% casein at room temperature and incubated overnight at 4 °C in primary antibody (Additional File 1: Table S1). Membranes were incubated in appropriate secondary antibody (Additional File 1: Table S1) diluted in 0.5% casein (1:20,000) with 0.005% SDS for 1 h at room temperature. Membranes were washed in 1 × TBS and water, and protein bands were detected using the multiplex Li-Cor Odyssey Infrared Imaging system (Li-Cor Biosciences,

Lincoln, NE, USA). Relative band intensity was quantified using ImageJ software (NIH).

For ELISA determination of Aβ levels, Immulon 4HBX plates were coated with 20 μg/μl of capture antibody (Additional File 1: Table S1) overnight at 4 °C. Plates were washed and blocked in Block ACE (Bio-Rad) (Additional File 1: Table S1) at 4 °C overnight. Plates were washed and loaded with SDS lysates or FA lysates (neutralized in Tris buffer) at predetermined dilutions (ranging from 1:300 for 3-month-old mice to 1:750 for 6-month-old mice). Following overnight incubation, plates were washed and incubated in capture antibody specific for Aβ42 or Aβ40. Following thorough washing, colorimetric assay was developed using TMB solution and detected using Spectramax ELISA reader. The data was analyzed using Softmax program.

RNAseq

RNA was extracted from frozen, pulverized forebrains using TRIzol reagent (Invitrogen). Extracted RNA was cleaned using RNeasy mini extraction kit with on-column DNase treatment (Qiagen). RNA quality was quantified with the Qubit RNA HS assay (Invitrogen). RNA quality was checked on an Agilent Bioanalyzer 2100 with the Eukaryote Total RNA Nano chip (Additional File 1: Table S1). Total RNA (1 μg) was used for sequencing library preparation using the Illumina TruSeq RNA library prep with polyA purification (Additional File 1: Table S1). Libraries were loaded at equimolar quantities and sequenced on paired-end, 75 bp runs on the Nextseq 500 (Illumina) with a goal of attaining a yield of 30–50 Mb of sequence per sample. RNA extraction and sequencing was performed with an aim to reduce batch effects.

RNAseq data analysis

FASTQ alignment, gene counts, and differential expression analysis

FASTQ files were aligned against the mouse genome (GRCm38 and GRCm38.94 annotation) using STAR v2.6.1a [17] to generate BAM files. BAM files were used to generate gene counts using Rsamtools and the summarizeOverlaps function with the GenomicAlignments package [18]. Differential gene expression analysis was performed with DESeq2 package using the "DESeq" function with default settings [19] which fits a generalized linear model for each gene. Subsequent Wald test *p*-values are adjusted for multiple comparisons using the Benjamini–Hochberg method (adjusted *p*-value, padj). Pair-wise changes in gene expression levels were examined between groups to identify differentially expressed genes (DEGs). DEGs were defined as an absolute log-2Fold Change ≥ 0.5 and an adjusted *p*-value ≤ 0.05.

Cell type signatures

Gene lists identifying cell-types within the brain and microglial and astrocytic subtype were obtained from previously published studies [20–26]. Using these gene lists, the geometric mean of the FPKM (fragments per kilobase of exon per million mapped fragments) for genes identified for each cell or cellular subtype was calculated on a per-animal basis. Group means were calculated, and between group significance values determined by one-way ANOVA. Outliers were removed from the group if their value fell outside of 1.5 times the inter-quartile range (IQR).

WGCNA

The WGCNA package in R [27, 28] was used to construct gene correlation networks from the expression data after filtering and removing genes with zero variance. Soft power settings were chosen using the "pickSoftThreshold" function within the WGCNA package. Networks were constructed separately for *APP* TG and nonTG samples. Adjacency matrices were constructed using expression data and these power settings with the "adjacency" function and a signed hybrid network. Module identification was performed using the "cutreeDynamic" function and a deepSplit setting of 2 with a minimum module size of 30 for all analyses. Modules with similar gene expression profiles were merged using the mergeModules function.

Functional annotation of DEGs, heatmap clusters, and WGCNA modules

Gene ontology enrichment analysis was performed with goseq v1.42.0 [29] to identify gene ontology categories and KEGG pathways that are affected for the given gene lists. For DEGs, up- and downregulated gene lists were analyzed separately. For WGCNA, gene lists from each module were used as input and GOseq analysis was performed for each module separately. Over-represented *p*-values were adjusted for multiple comparisons using the Benjamini–Hochberg adjustments for controlling false-discovery rates. An enrichment score was calculated by an observed-over-expected ratio of

$$(DEG/totalDEG)/(CategoryTotal/GeneTotal)$$

where DEG represents the total number of DEGs or module genes within the GO or KEGG category, totalDEG represents the total number of DEGs or module genes; CategoryTotal represents the total number of genes within the GO or KEGG category and GeneTotal represents the total number of genes examined. GO terms and KEGG pathways are filtered for *p*-values

adjusted for multiple comparisons (BHadjust) < 0.05, enrichment scores > 1, and total number of genes within the category > 5.

Gene lists to annotate WGCNA modules and identify microglia subtype signatures were identified from previously published studies [20, 21, 23–26, 30]. Gene overlap analysis was conducted with the GeneOverlap package in R (http://shenlab-sinai.github.io/shenlab-sinai/). GeneOverlap uses Fisher's exact test to calculate the *p*-value for significance testing as well as calculating the odds ratio. goseq was used for GO and KEGG pathway analysis of genes within each module filtering for those terms with *p*-values < 0.05, enrichment scores > 1, and total number of genes within the category > 5.

Correlation analysis from human brains and mouse brains

To assess *GNGT2* and *ABI3* for correlation in human brain, RNAseq expression measures collected from two datasets representing three brain regions (TCX = temporal cortex, CER = cerebellum, DLPFC = dorsolateral prefrontal cortex) were obtained from the AD-knowledge portal (Mayo RNAseq [31] and ROSMAP [32] studies). The AMP-AD consortium previously reprocessed the raw format RNASeq data from these two studies through a consensus alignment, counting and quality control pipeline (RNAseq Harmonization Study). The reprocessed gene counts and associated metadata were downloaded and underwent further quality control, followed by CQN normalization of the raw counts for the 631 ROSMAP, 259 Mayo RNAseq TCX, and 246 Mayo RNAseq CER samples that remained. For ROSMAP, four samples were excluded due to missing metadata, one sample removed due to inconsistent sex between provided metadata and expression of Y chromosome genes, and three samples removed based on being outliers (> 4 SD from mean, PC1 or PC2) in principal components analysis of the reprocessed gene counts (counts per million). For Mayo RNAseq, samples were excluded from the RNASeq datasets based on quality control (QC) outcomes provided in the metadata files. An additional 3 samples were removed due to being gene expression outliers following principal components analysis (> 4 SD from mean, PC1 or PC2) of the reprocessed gene counts (counts per million). CQN normalized gene counts for *ABI3* and *GNTG2* were extracted for each dataset and plotted in R-3.6.0 using ggplot2. The correlation in the expression between the two genes was assessed using the cor.test function (spearman) in R-3.6.0.

To examine the correlation between *Gngt2* and *Abi3* in the mouse cortex, bam sequencing alignment files from the TgCRND8 and rTg4510 mouse models were downloaded from the *MAPT* and *APP* mouse model study at Synapse (10.7303/syn3157182). The gene counting step was performed with the summarizeOverlaps functions in the GenomicAlignments package [18] and counts were subsequently converted to FPKM with the DESeq2 package [19] in R 4.1.0. Gngt2 and Abi3 FPKM values were extracted and plotted in R using the ggscatter function and Spearman correlation method in the ggpubr package (https://CRAN.R-project.org/package=ggpubr).

In situ hybridization (RNAscope®, Advanced Cell Diagnostics, Newark, CA) and combined in situ hybridization/immunohistochemistry

For in situ hybridization, 5-µm-thick formalin-fixed paraffin-embedded tissue sections were rehydrated in xylene and series of ethanol solutions (100, 90, and 70%). Slides were incubated with RNAscope® Hydrogen peroxide for 10 min at room temperature, followed by antigen retrieval in steam for 15 min using RNAscope® 1 × target retrieval reagent. After incubation in 10% ethanol for 3 min, slides were air dried at 60 °C. Subsequently, slides were incubated with RNAscope® Protease plus reagent for 30 min at 40 °C in a HybEZ™ oven, followed by 3 washes in distilled water. Slides were then incubated with the following RNAscope® probes (Mouse Abi3 (Cat No. 539161), human ABI3-O1 (Cat No. 549711)) for 2 h at 40 °C in a HybEZ™ oven. Following washes with 1X Wash buffer, slides were incubated with RNAscope®AMP1 solution for 30 min at 40 °C followed by series of washes in AMP buffers and incubation in RNAscope® Fast RED-B and RED-A mixture (1:60 ratio) for 10 min at room temperature. For immunohistochemistry double labeling, sections were incubated in Impress® horse serum (2.5%, Vector Laboratories) solution for 20 min, followed by a 5-min incubation in 2% FBS/0.1 M Tris, pH 7.6. Iba-1 (1:500; Wako) was diluted in 2% FBS/0.1 M Tris, pH 7.6 and allowed to incubate on sections overnight at 4 °C. Slides were then washed and incubated in ImmPress® anti-rabbit IgG plus reagent (Vector Laboratories) for 30 min at room temperature. After two washes in 0.1 M Tris, pH 7.6 for 5 min each, immunocomplexes were visualized using the chromogen 3,3′-diaminobenzidine (DAB kit; KPL, Gaithersburg, MD). Tissue sections were counterstained with hematoxylin (Sigma-Aldrich, St. Louis, MO), air dried at 60 °C for 15 min, and cover slipped using EcoMount™ mounting medium (Biocare Medical).

In vitro expression and phosphorylation analysis of ABI3

Plasmid encoding for *ABI3* (NM_016428) was purchased from OriGene (Catalog# RC202853). Site-directed mutagenesis in *ABI3* was performed, and resulting clones were Sanger sequenced to confirm the presence of mutation. HEK293T cells were grown in DMEM media supplemented with 10% fetal bovine serum (Gibco) and 1%

penicillin/streptomycin (Life Technologies) and transiently transfected by $CaCl_2$ method. Forty-eight hours later, the transfected cells were lysed in RIPA buffer (Fisher) supplemented with EDTA-free Protease Inhibitor Cocktail and phosphatase inhibitor tablets (Sigma-Aldrich). Protein extracts were loaded on Bis–Tris precast gels (Bio-Rad) were transferred on PVDF membrane for Western blotting with the Li-Cor system. ABI3 was detected with the following antibodies according to the experiment: FLAG-M2 (Sigma-Aldrich), N terminal Anti-ABI3 (Sigma-Aldrich), or anti-ABI3 209F (manufactured by Pacific Immunology Corp using the peptide sequence 195-PVVPDGRLSAASSAF-209). Lambda Protein Phosphatase (NEB) assay was performed as described by the supplier. Briefly, ABI3 HEK-transfected cells were lysed in PBS 0.1% NP-40 in the presence of EDTA-free protease and phosphatase inhibitors. Cytoplasmic proteins fractions were used for the reaction and analyzed by Western blotting.

Statistical analysis

Detailed description of statistics is provided in each figure legend and in the methods section. Statistical analysis was done using GraphPad Prism.

Results

ABI3 is expressed in microglia and neurons in mice and humans

Recent reports have confirmed *ABI3* as an AD risk gene [6–8]. *ABI3* has been reported to be a microglia-specific gene using single-cell RNAseq [12, 20]. Bulk RNAseq data reveals increased levels of ABI3 RNA relative to control cohorts in both the temporal cortex and cerebellum of human patients and in mouse models of amyloid and tau pathologies [6]. In AD brains, ABI3 expression is significantly upregulated relative to controls ($p = 4.47E-03$) [6]. We further confirmed this in aging cohorts of *APP* TgCRND8 (TG) mice relative to nontransgenic (NonTG) age-matched mice (Fig. 1a; Additional File 2: Table S2). It is notable that increasing plaque burden, and not necessarily age, seems to be associated with increased Abi3 expression (Fig. 1a). In *MAPT* transgenic rTg4510 mice, the RNA levels of Abi3 increased in 4.5-month-old tau expressing mice but reduced to levels comparable to nonTG littermates at 6 months (Fig. 1b; Additional File 3: Table S3).

To provide cellular localization information complementary to this quantitative bulk RNAseq data, we used RNAscope to localize Abi3 expression in mouse and human tissues (Fig. 1c-f, Additional File 4: Fig. S1). In AD patients, we observed Abi3 transcript in Iba1-immunopositive microglia as well as in Iba-1 nonreactive cells in the grey matter, which are presumed to be neurons based on size and location (Fig. 1c1, c2; Additional File 4: Fig. S1a-f). Specificity for the RNA in situ hybridization signal was confirmed by using brain tissue from *APP* mice completely lacking the *Abi3* locus (Fig. 1d1, d2; Additional File 4: Fig. S1g-l). In 6-month-old and 18-month-old *APP* TgCRND8 mice, we observed Abi3 + microglia in the cortex and in the white matter tracts (Fig. 1e1, f1, f2; Additional File 4: Fig. S1m-x). Similar to human cases, we noted Abi3 + cells in the neuronal layers in the cortex and hippocampus in these mice (Fig. 1e2, f2). Overall, RNAscope confirmed the presence of Abi3 RNA in both microglial and non-microglial cells in AD and an *APP* mouse model.

ABI3 and GNGT2 genes are co-regulated in *APP* mouse models and in AD

To elucidate how Abi3-specific immune signaling contributes to the neurodegenerative cascade in AD, we obtained the $Abi3^{-/-}$ mice from Jax Labs (Stock #028180). While using bulk RNAseq to characterize these mice, we serendipitously discovered that the levels of another gene, *Gngt2*, were dramatically reduced to the same extent as *Abi3* (Additional File 5: Fig. S2a). We surveyed the gene maps and found that mouse *Abi3* locus overlaps with two other genes on chromosome 11—microglia-specific G protein gamma transducing activity polypeptide 2 (*Gngt2*) and *Phospho-1* (Additional File 5: Fig. S2b). We also confirmed that in humans, the arrangement of the *ABI3*, *GNGT2* and *PHOSPHO-1* genes is conserved, albeit being on chromosome 17. Using data from UCSC genome browser, we discovered that the Velocigene targeted deletion in the *Abi3* locus knocked out both *Abi3* and *Gngt2* (Additional File 5: Fig. S2b). In subsequent sections, we will refer to these mice as *Abi3-Gngt2*$^{-/-}$. Notably, we did not find any changes in Phospho-1 transcript levels in these mice.

Given that *Abi3* and *Gngt2* genes are overlapping, we hypothesized that their expression could be correlated. Using RNAseq data from the AMP-AD consortium, we investigated the concordance between the expression patterns of *Abi3* and *Gngt2*. We found that *ABI3* and *GNGT2* genes were co-regulated in three distinct AD patient cohorts: temporal cortex samples of Mayo Clinic AD cohort (Mayo TCX: $\rho = 0.644$, $p = 2.2e-16$) (Fig. 2a), cerebellar samples of Mayo Clinic AD cohort (Mayo CER: $\rho = 0.556$, $p = 2.2e-16$) (Fig. 2b) and prefrontal cortex samples of Religious Orders Study and Rush Memory and Aging Project AD cohort (ROSMAP; $\rho = 0.328$, $p = 2.2e-16$) (Fig. 2c). We also confirmed that *Abi3* and *Gngt2* genes are co-regulated in the *APP* transgenic TgCRND8 mice (Fig. 2d, $\rho = 0.625$, $p = 7.31-06$) and in *MAPT* transgenic rTg4510 mice (Fig. 2e, $\rho = 0.554$, $p = 0.018$). The nonTG littermates of these mice showed

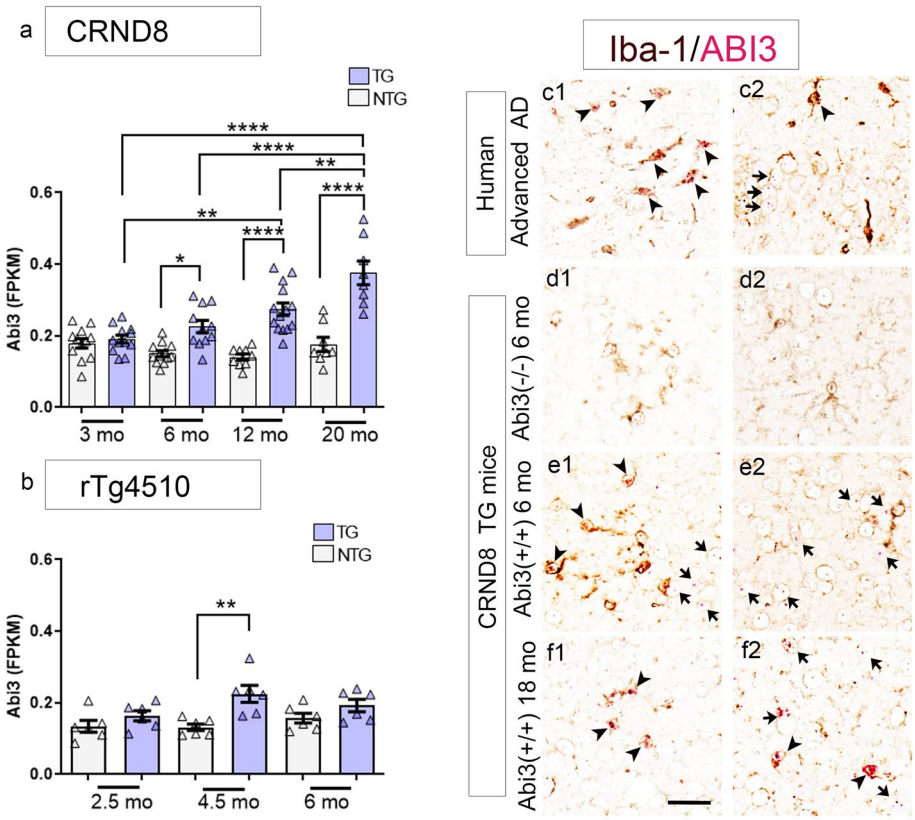

Fig. 1 ABI3 RNA is expressed in microglia and neurons in mice and humans. **a**, **b** Abi3 RNA levels (FKPM) plotted across different ages in *APP* CRND8 mice (**a**) and *MAPT* rTg4510 mice (**b**).

Source data obtained from Mayo RNAseq study (AD Knowledge Portal: https://adknowledgeportal.org). $n = 9$–14 (a) and $n = 6$ per genotype/age. **b**. One-way ANOVA, ****$p < 0.0001$; **$p < 0.01$; *$p < 0.05$. **c**–**f** In situ hybridization was done to detect ABI3 (Fast Red; red color) RNA on human and mouse paraffin-embedded brain sections immunostained with anti Iba-1 antibody (brown color). Arrowheads indicate Iba-1 (microglia) associated in situ signal and arrows indicate in situ signal in non-Iba-1 cells. $n = 3$ (human AD cases, 6-month-old TG-*Abi3-Gngt2*$^{-/-}$ mice and 6-month-old TG-*Abi3-Gngt2*$^{+/+}$ mice) and $n = 1$ (18-month-old TgCRND8 mice). Representative of two independent experimental replicates. Two separate images are shown from each cohort, indicated as c1-c2, d1-d2, e1-e2, f1-f2. Additional representative images are available in Additional File 4 Fig. S1. NonTG, nontransgenic; TG, transgenic

no correlation between *Abi3* and *Gngt2* expression. In addition, we investigated 96 additional mouse transcriptomic datasets [33, 34] and in 26 of these cohorts, we found that *Abi3* and *Gngt2* were both differentially regulated. Among these 26 cohorts, *Abi3* and *Gngt2* expression changes were concordant in 24 studies (Additional File 6: Table S4), showing that these genes are consistently co-regulated across different mouse models and experimental cohorts. Collectively, these analyses show that expression of *ABI3* and *GNGT2* genes are in a tight co-expression network in AD and AD mouse models.

Loss of *Abi3-Gngt2* induces reactive gliosis and a glial gene signature typically associated with AD

We evaluated baseline gliosis in the parental *Abi3-Gngt2*$^{-/-}$ line. Using Iba-1 immunohistochemistry, we found that at 3 months of age, the heterozygous *Abi3-Gngt2*$^{+/-}$ mice showed reduced hippocampal microgliosis compared to wild type *Abi3-Gngt2*$^{+/+}$ mice ($p < 0.01$ in hippocampus) and *Abi3-Gngt2*$^{-/-}$ mice (ns association) (Fig. 3a–c). At 6 months of age, we noticed an interesting gene-dosage-dependent dichotomy in microgliosis in the *Abi3-Gngt2* lines. The heterozygous *Abi3-Gngt2*$^{+/-}$ mice showed higher Iba-1 reactivity relative to WT *Abi3-Gngt2*$^{+/+}$ mice ($p < 0.05$ in cortex) and *Abi3-Gngt2*$^{-/-}$ mice ($p < 0.01$ in cortex and $p < 0.05$ in hippocampus) (Fig. 3d–f). There were no significant differences in microgliosis between the WT *Abi3-Gngt2*$^{+/+}$ and *Abi3-Gngt2*$^{-/-}$ mice at this age (Fig. 3d–f).

At 3 months of age, GFAP-reactive gliosis levels in *Abi3-Gngt2*$^{-/-}$ mice showed increased trend relative to WT *Abi3-Gngt2*$^{+/+}$ and heterozygous *Abi3-Gngt2*$^{+/-}$ mice ($p < 0.05$ in cortex) (Fig. 3g–i). At 6 months of age,

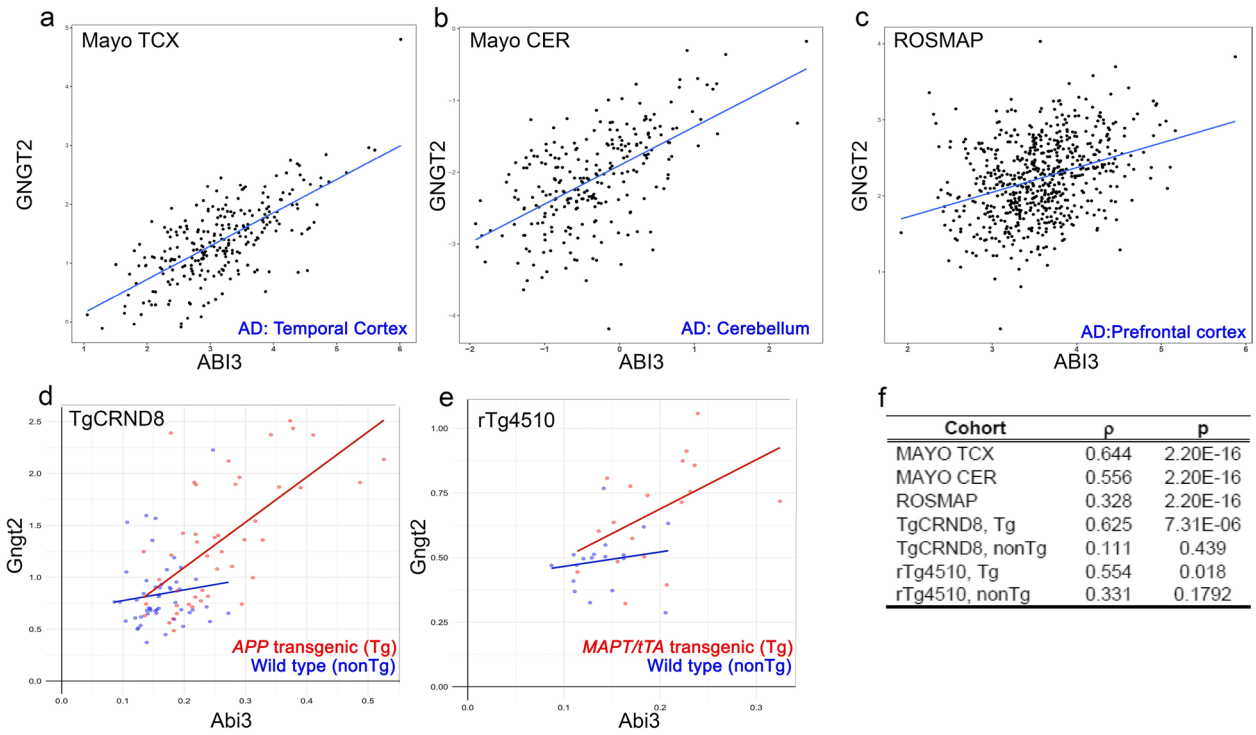

Cohort	ρ	p
MAYO TCX	0.644	2.20E-16
MAYO CER	0.556	2.20E-16
ROSMAP	0.328	2.20E-16
TgCRND8, Tg	0.625	7.31E-06
TgCRND8, nonTg	0.111	0.439
rTg4510, Tg	0.554	0.018
rTg4510, nonTg	0.331	0.1792

Fig. 2 ABI3 and GNGT2 genes are in a co-regulatory expression network. **a**–**c** Graphs showing co-regulation of ABI3 and GNGT2 RNA from AD patients. Data from Mayo AD cohorts (temporal cortex, TCX and cerebellum, CER) and ROSMAP AD cohorts obtained from AD Knowledge Portal (https://adknowledgeportal.org). **d**, **e** Graphs showing co-regulation of Abi3 and Gngt2 RNA from *APP* TgCRND8 and *MAPT* rTg4510 mice obtained from AD Knowledge Portal (https://adknowledgeportal.org). **f** Table depicting the correlation coefficient (ρ) and *p*-values adjusted for multiple testing for cohorts depicted in **a**–**e**. Tg, transgenic for *APP* (**d**) or *MAPT/tTA* (**e**); nonTg, nontransgenic background strain matched mice (**d**, **e**). Each datapoint indicates individual sample (**a**–**e**). *x* and *y* axes denote FPKM values of ABI3 and GNGT2 respectively

the astrocyte burden continued to remain elevated in the *Abi3-Gngt2*$^{-/-}$ mice relative to WT *Abi3-Gngt2*$^{+/+}$mice ($p < 0.05$ in cortex and hippocampus) and heterozygous *Abi3-Gngt2*$^{+/-}$ mice ($p < 0.05$ in hippocampus) (Fig. 3j–l). This shows that complete loss of function of the *Abi3* locus results in early astrocytosis that progresses as the mice age.

We performed bulk RNAseq from the forebrains of 3-month-old *Abi3-Gngt2* mice (Fig. 4; Additional File 7: Fig. S3). Relative to WT mice, the upregulated RNAs in the *Abi3-Gngt2*$^{-/-}$ mice were predominantly microglia-specific, such as C-type lectin domain family 7 member A (Clec7a/Dectin 1), Macrophage Expressed 1 (Mpeg1), Natural resistance-associated macrophage protein 1 (Slc11a1/Nramp1), Lymphocyte Antigen 86 (Ly86) and Olfactomedin-like 3 (Olfm13) (Fig. 4a,b). Downregulated RNAs included Abi3, Gngt2, G Protein-Coupled Receptor 179 (Gpr179), and TNF Receptor Superfamily Member 1B (Tnfrsf1b) (Fig. 4a,b). Analysis of the heterozygous *Abi3-Gngt2*$^{+/-}$ mice relative to WT *Abi3-Gngt2*$^{+/+}$ mice revealed only one significantly altered (downregulated) gene—Protocadherin Gamma Subfamily A 5 (Pcdha5)—that is involved in establishing and maintaining intercellular connections in the brain (Additional File 7: Fig. S3a). Pathway analysis of the differentially expressed gene sets in *Abi3-Gngt2*$^{-/-}$ mice relative to WT mice revealed the involvement of immune pathways, such as granulocyte (GO:0071621) and leukocyte chemotaxis (GO:0030595), proliferation of mononuclear leukocytes (GO:0032943), and

(See figure on next page.)

Fig. 3 Immune activation in *Abi3-Gngt2*$^{-/-}$ mice. Representative images of Iba-1 reactive microglia (**a**–**f**) and GFAP-reactive astrocyte (**g**–**l**) in 3-month-old or 6-month-old mice with WT (+/+), heterozygous (+/−), or KO (−/−) of *Abi3-Gngt2* genes. Quantitation of the Iba-1 or GFAP staining from cortex or hippocampus is provided in corresponding panels on the right side. $N = 6$ mice (**a**–**f**), 7 mice (**g**–**l**). Scale bar, 50 µm. Clear symbols denote female mice and filled symbols denote male mice. Data represents mean ± sem. One-way ANOVA; ***$p < 0.001$; **$p < 0.01$; *$p < 0.05$. KO, knockout; Het, heterozygous; WT, wild type

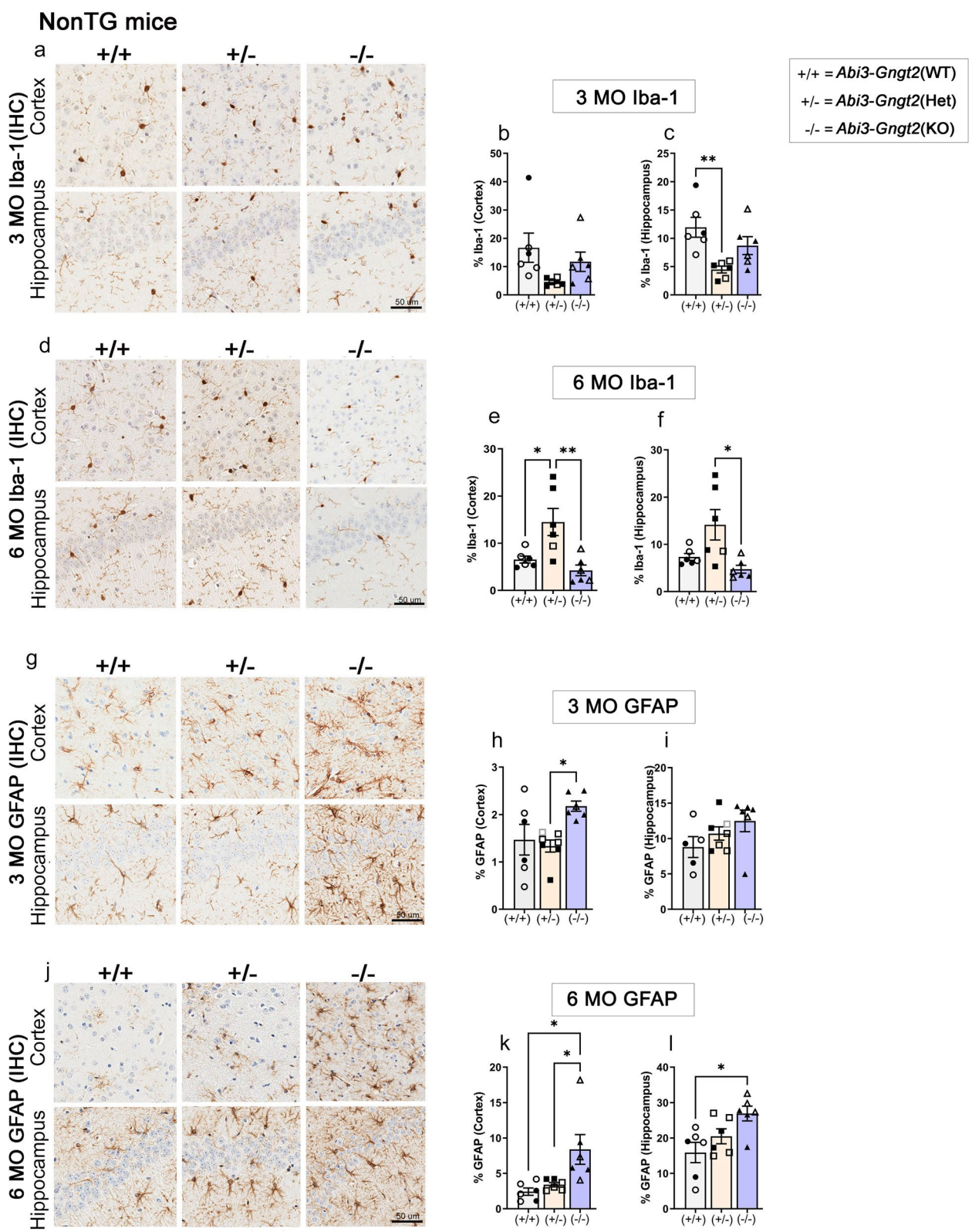

Fig. 3 (See legend on previous page.)

leukocyte-mediated immunity (GO:0002443) (Fig. 4c). The cell types most affected in *Abi3-Gngt2*$^{-/-}$ mice were microglia which showed increase in these mice relative to WT and heterozygous *Abi3-Gngt2*$^{+/-}$ mice ($p < 0.05$) (Fig. 4d). There was a specific reduction in neuronal gene counts in *Abi3-Gngt2*$^{-/-}$ mice ($p < 0.01$ relative to WT mice) and in heterozygous mice ($p < 0.001$ relative to both WT and *Abi3-Gngt2*$^{-/-}$ mice) (Fig. 4d). No significant changes in astrocyte or oligodendrocyte-specific gene counts were seen among the three groups (Fig. 4d). Surprisingly, the *Abi3-Gngt2*$^{-/-}$ mice showed induction of the amyloid/AD-associated PIG network, even in the absence of Aβ ($p < 0.01$ relative to both WT and heterozygous mice) (Fig. 4e). We also observed suggestive upregulated trends in the DAM, MGnD, ARM, and A1 co-expression networks in the *Abi3-Gngt2*$^{-/-}$ mice (Fig. 4e). Weighted gene co-expression network analysis (WGCNA) identified several gene modules correlating the *Abi3-Gngt2* genotype with the gliosis phenotype (Fig. 4f). The hub genes of selected modules that specifically correlated with the *Abi3-Gngt2*$^{-/-}$ genotype and gliosis include Unc93b1 (antiquewhite2) and immunoglobulin kappa variable 10–96 (coral2) (Additional File 7: Fig. S3b-d). The antiquewhite2 module is especially relevant to AD pathophysiology as the module members, Ctss, Siglech, Csf3r, Ly86, and C1qc, have been reported in both mouse models and humans (Additional File 7: Fig. S3b) [35]. These genes are also reported to be associated with pathologic signatures in AD, most notably DAM and MGnD [24, 25] and PIG [21] (Additional File 7: Fig. S3e). It was also highly associated with several immune and autoimmune conditions such as Staphylococcus infection and primary immunodeficiency as well as neurodegenerative diseases such as prion disease (Additional File 7: Fig. S3f). Overall, RNAseq data shows an inflammatory gliosis profile corresponding to AD-typical gene expression patterns in *Abi3-Gngt2*$^{-/-}$ mice, even in the absence of Aβ.

Reduction in Aβ levels in *APP* mice lacking *Abi3-Gngt2*

We then examined how complete insufficiency or haploinsufficiency of the *Abi3* locus alters Aβ plaque pathology in *APP* transgenic CRND8 mice. Transgenic *APP* mice (referred as "TG") that are wild type (+/+), heterozygous (+/−), or knocked out (−/−) for *Abi3-Gngt2* genes were aged to 3 and 6 months and the Aβ levels assessed by immunohistochemistry and biochemical analysis (Fig. 5, Additional File 8: Fig. S4). There was no change in APP expression levels in these bigenic TG-*Abi3-Gngt2* colonies (Additional File 8: Fig. S4a-b). At 3 months, both heterozygous *Abi3-Gngt2*$^{+/-}$ ($p < 0.05$) and *Abi3-Gngt2*$^{-/-}$ ($p < 0.01$) mice showed reduced Aβ plaques relative to *APP* transgenic mice wild type for *Abi3-Gngt2* (Fig. 5a,b). Concurrently, there was a non-significant reduction in the number of Thioflavin S cored plaques in the TG-*Abi3-Gngt2*$^{-/-}$ mice (Fig. 5c,d). Biochemical analysis showed significant reduction of FA associated insoluble Aβ42 and Aβ40 levels in both TG-*Abi3-Gngt2*$^{+/-}$ (Aβ42: $p < 0.01$; Aβ40: $p < 0.05$) and TG-*Abi3-Gngt2*$^{-/-}$ (Aβ42: $p < 0.001$; Aβ40: $p < 0.05$) mice relative to TG-*Abi3-Gngt2*$^{+/+}$ mice (Fig. 5e,f). In the SDS detergent-soluble fraction, both Aβ42 and Aβ40 values were reduced in TG-*Abi3-Gngt2*$^{-/-}$ mice ($p < 0.05$) while only Aβ42 was significantly reduced in TG-*Abi3-Gngt2*$^{+/-}$ mice ($p < 0.05$) relative to TG-*Abi3-Gngt2*$^{+/+}$ mice (Fig. 5g,h). We did not observe major changes in ubiquitin labeling of the Aβ plaques across all the *Abi3* genotypes (Additional File 8: Fig. S4c).

At 6 months of age, complete deletion of *Abi3-Gngt2* resulted in reduced total Aβ plaque burden (Fig. 5i,j, $p < 0.05$) as well as number of cored plaques (Fig. 5k,l, $p < 0.01$) in TG-*Abi3-Gngt2*$^{-/-}$ mice relative to TG-*Abi3-Gngt2*$^{+/+}$ mice. Notably, though the immunohistochemical plaque burden was similar between TG-*Abi3-Gngt2*$^{+/-}$ and TG-*Abi3-Gngt2*$^{+/+}$ mice (Fig. 5i,j), the former group showed lower thioflavin S (ThioS) plaque number compared to the latter group (Fig. 5k,l, $p < 0.05$). The FA and SDS level of Aβ was mostly equivalent among all the

(See figure on next page.)

Fig. 4 Unbiased transcriptomic analysis of *Abi3-Gngt2*$^{-/-}$ mice reveal upregulation of immune pathways and disease-related gene expression patterns. **a**–**c** Volcano plot (**a**), list of top 5 upregulated and top 5 downregulated genes (based on fold change; orange, upregulated genes, blue, downregulated genes) (**b**) and GO pathways based on enriched genes (**c**) in 3-month-old *Abi3-Gngt2*$^{-/-}$ mice relative to *Abi3-Gngt2*$^{+/+}$ mice. Orange dots, upregulated genes; blue dots, downregulated genes (**a**). FC, fold change; DEG, differentially expressed genes; padj, *p*-values adjusted for multiple comparison. **d** Cell type population analyses indicating changes in microglia, astrocytes, neurons, and oligodendrocyte populations in 3-month-old mice with WT (+/+), heterozygous (+/−), or KO (−/−) of *Abi3-Gngt2* locus. One-way ANOVA, ***$p < 0.001$, **$p < 0.01$, *$p < 0.05$. **e** Gene expression signatures for microglia or astrocyte functional subtypes in 3-month-old mice with WT (+/+), heterozygous (+/−), or KO (−/−) of *Abi3-Gngt2* locus. These cell-type-specific signatures were identified in previous studies [21–28]. One-way ANOVA, **$p < 0.01$. **f** WGCNA gene co-expression modules correlating with specific experimental traits (Iba-1 burden, GFAP burden, and *Abi3-Gngt2*$^{-/-}$ genotype) shown. Correlation of modules to different experimental traits is colored in a heatmap (red, positive correlation; blue, negative correlation). Modules with *p*-values < 0.05 and correlation value < -0.5 or > 0.5 are indicated in colored tiles (see scale on right). Cell-type-specific gene lists were used to identify genes with significant overlap (odds ratio, see scale on right) within the modules. The heatmap is colored by the value of the odds ratio; higher the odds ratio of association, warmer the color. Grey squares indicate non-significant ($p > 0.05$, odds ratio < 2) overlaps in the gene lists. All *p*-values adjusted for multiple comparisons (padj). $n = 4$ mice (2 males, 2 females) per *Abi3-Gngt2* genotype except 1 outlier removed in **d**, **e**

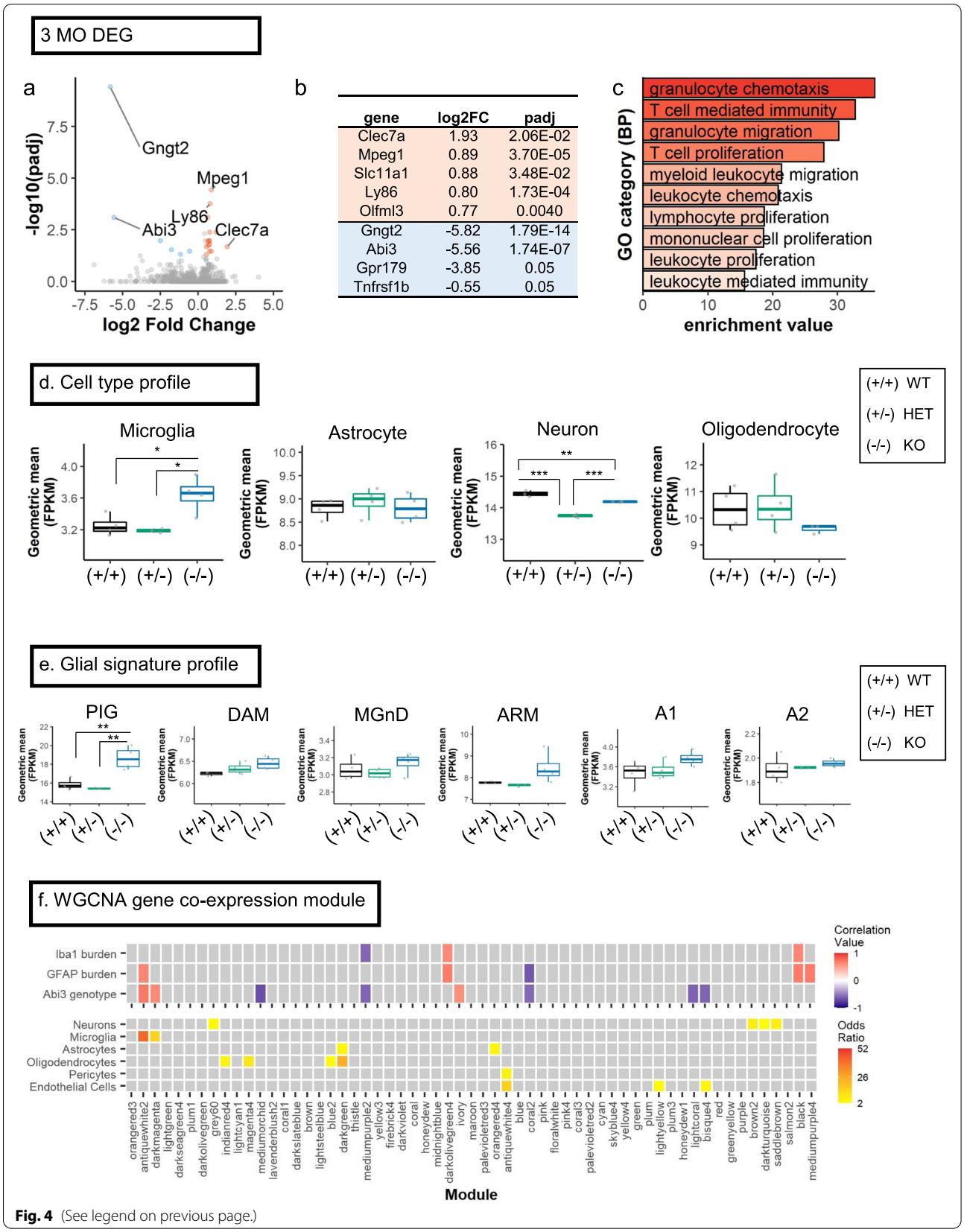

Fig. 4 (See legend on previous page.)

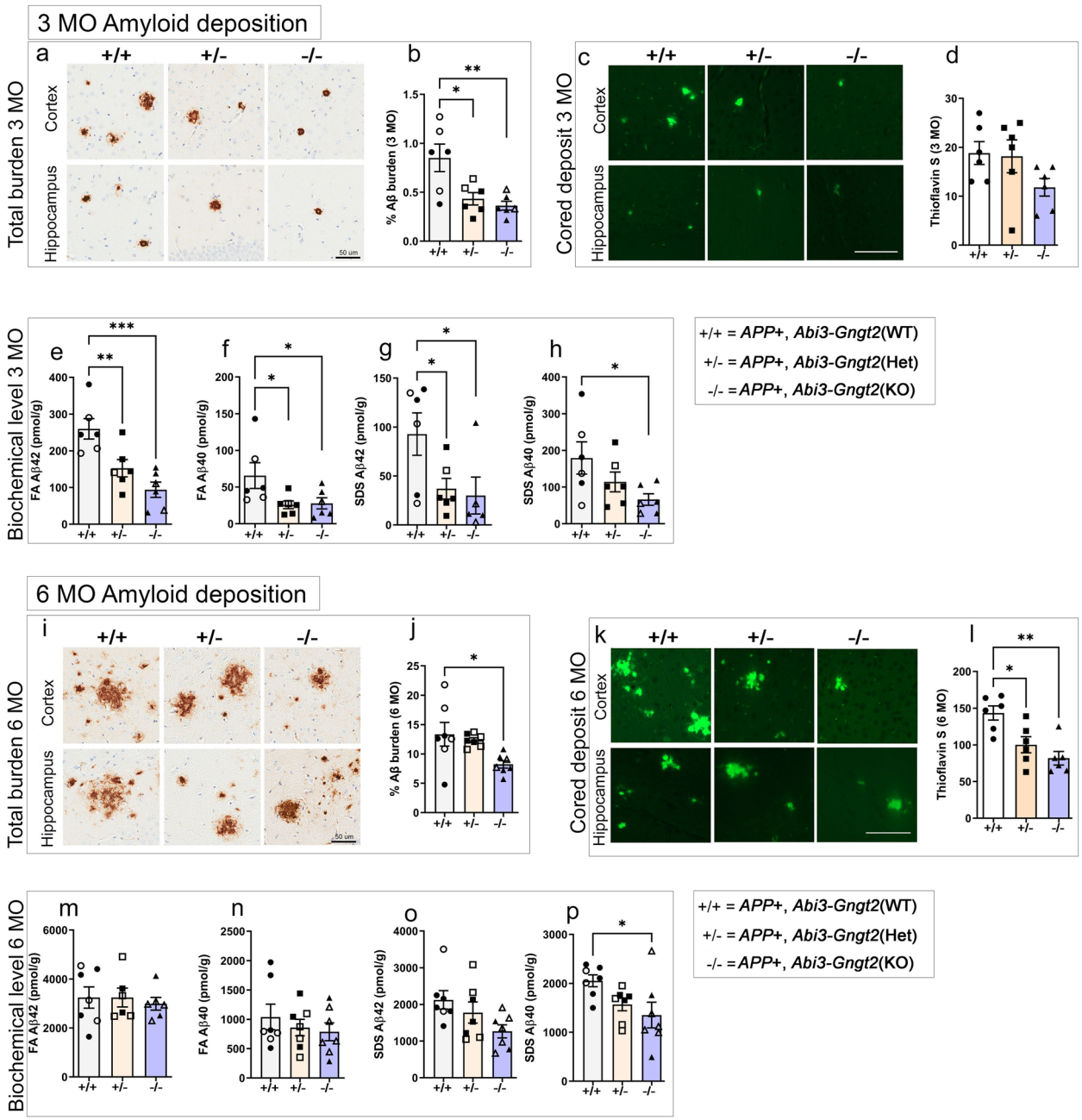

Fig. 5 Loss of Abi3-Gngt2 expression ameliorates Aβ in a gene-dosage manner. **a**, **b** Representative immunohistochemical images of total Aβ plaque burden and quantification in 3-month-old *APP* TG mice with WT (+/+), heterozygous (+/−), or KO (−/−) of *Abi3-Gngt2* locus. **c**, **d** Representative images of thioflavin S-stained cored Aβ plaques and quantitation in 3-month-old *APP* TG mice with WT (+/+), heterozygous (+/−), or KO (−/−) of *Abi3-Gngt2* locus. **e**–**h** Biochemical levels of formic acid (FA) solubilized and detergent (SDS) soluble Aβ42 and Aβ40 in 3-month-old *APP* TG mice with WT (+/+), heterozygous (+/−), or KO (−/−) of *Abi3-Gngt2* locus. **i**, **j** Representative immunohistochemical images of total Aβ plaque burden and quantification in 6-month-old *APP* transgenic mice with WT (+/+), heterozygous (+/−), or KO (−/−) of *Abi3-Gngt2* locus. **k**, **l** Representative images of thioflavin S-stained cored plaques and quantitation in 6-month-old *APP* TG mice with WT (+/+), heterozygous (+/−), or KO (−/−) of *Abi3-Gngt2* locus. **m**–**p** Biochemical levels of FA solubilized and SDS soluble Aβ42 and Aβ40 in 6-month-old *APP* TG mice with WT (+/+), heterozygous (+/−), or KO (−/.−) of *Abi3-Gngt2* locus. *N* = 6 mice (**a**–**h**), 7 mice (**i**, **j**, **m**-**p**), 6 mice (**k**, **l**). Scale bar, 50 µm (**a**, **i**); 100 µm (**c**, **k**). Clear symbols denote female mice and filled symbols denote male mice (except panel **d**, **k**). *n* = 3 females, 3 males (3 months) and *n* = 3 females, 4 males (6 months). Data represents mean ± sem. One-way ANOVA; ***$p < 0.001$; **$p < 0.01$; *$p < 0.05$

groups except for reduction in SDS-associated Aβ40 in TG-*Abi3-Gngt2*$^{-/-}$ mice relative to TG-*Abi3-Gngt2*$^{+/+}$ mice (Fig. 5m–p, $p<0.05$). The patterns of ubiquitin staining around plaques appeared unchanged across the *Abi3* genotypes (Additional File 8: Fig. S4d).

We generated an additional cohort of 9-month-old TG-*Abi3-Gngt2*$^{+/-}$ mice for neuropathological comparisons with age-matched TG-*Abi3-Gngt2*$^{+/+}$ mice. We found no changes in Aβ burden, astrocytosis (GFAP), microgliosis (Iba-1 and cd11b), or ubiquitin staining patterns between these two cohorts of mice at this age (Additional File 8: Fig. S4e-m).

Alterations in gliosis, especially astrocyte dysfunction, impacts synaptic health [36]. To survey how amyloid plaques and gliosis in this model affect neuronal health, we evaluate several pre- and post-synaptic proteins at 3 months of age in the TG mice. Consistent with the reduction in Aβ levels, we saw improved synaptic function as exemplified by increased synaptophysin level in both TG-*Abi3-Gngt2*$^{+/-}$ mice ($p<0.05$) and TG-*Abi3-Gngt2*$^{-/-}$ mice ($P<0.01$) (Additional File 9: Fig. S5a-b). We observed an insignificant trend in increased PSD95 levels in TG-*Abi3-Gngt2*$^{-/-}$ mice while levels of synaptogyrin3 and spinophilin were unaltered in the three genotypes rested (Additional File 9: Fig. S5c-h). There was a reduction in vGlut1 ($p<0.01$ in TG-*Abi3-Gngt2*$^{+/-}$; $p<0.05$ in TG-*Abi3-Gngt2*$^{-/-}$), GluR1 ($p<0.05$ in TG-*Abi3-Gngt2*$^{+/-}$), and GluR2 levels (trend in TG-*Abi3-Gngt2*$^{-/-}$) compared to TG-*Abi3-Gngt2*$^{+/+}$ mice, signifying dysfunctional glutamatergic signaling (Additional File 9: Fig. S5i-n).

Gene dose-dependent regulation of inflammatory profile in TG-*Abi3-Gngt2*$^{-/-}$ mice

Aβ levels are generally well-correlated with immune activation indicated by microgliosis and astrocytosis [3]. Thus, we predicted lower burden of microglia (Iba-1 immunoreactivity) and astrocytes (GFAP immunoreactivity) in TG-*Abi3-Gngt2*$^{-/-}$ mice because these mice showed robust Aβ reduction at 3 months and 6 months of age. Surprisingly, we found that at both ages, the TG-*Abi3-Gngt2*$^{-/-}$ mice showed similar levels of Iba-1 reactive microgliosis compared to TG-*Abi3-Gngt2*$^{+/+}$ mice (3 months: Fig. 6a–c; 6 months: Fig. 6d–f). The heterozygous TG-*Abi3-Gngt2*$^{+/-}$ mice showed decreased cortical microglia at 3 months compared to TG-*Abi3-Gngt2*$^{-/-}$ mice (Fig. 6a–c; $p<0.05$), but this normalized to equivalent levels by 6 months of age (Fig. 6d–f). The patterns of astrocyte burden reflected a differential scenario across the three *Abi3* genotypes. At 3 months of age, the TG-*Abi3-Gngt2*$^{+/-}$ mice had significantly lower astrocytosis compared to both TG-*Abi3-Gngt2*$^{+/+}$ ($p<0.01$ in cortex; $p<0.001$ in hippocampus) and TG-*Abi3-Gngt2*$^{-/-}$ mice ($p<0.001$ in cortex; $p<0.01$ in hippocampus) (Fig. 6g–i). At 6 months of age, these differences normalized in the cortex but hippocampal GFAP burden in TG-*Abi3-Gngt2*$^{+/-}$ mice was higher than both TG-*Abi3-Gngt2*$^{+/+}$ or TG-*Abi3-Gngt2*$^{-/-}$ mice (Fig. 6j–l). There was no significant difference in astrocytosis burden between the TG-*Abi3-Gngt2*$^{+/+}$ or TG-*Abi3-Gngt2*$^{-/-}$ mice in 3-month or 6-month-old cohorts (Fig. 6g–i, j–l), indicating that reduction of Aβ did not ameliorate the existing astrocytic phenotype inherent in the *Abi3-Gngt2* line. Overall, the immunohistochemistry data suggests a biphasic age-dependent response of the astrocytes and microglia in *APP* mice in relation to *Abi3-Gngt2* gene dosage.

We performed bulk RNAseq from forebrains of 3-month-old TG-*Abi3-Gngt2* mice (Fig. 7, Additional File 10: Fig. S6). Relative to the *TG-Abi3-Gngt2*$^{+/+}$ mice, the *TG-Abi3-Gngt2*$^{-/-}$ mice showed lower Abi3 and Gngt2 as expected (Fig. 7a,b). Other genes that were downregulated in the *TG-Abi3-Gngt2*$^{-/-}$ mice are *Adgrf3* (Adhesion G Protein-Coupled Receptor F3), *S100a8*, and *S100a9* (S100 Calcium-Binding Protein members A8 and A9). Among the genes that were upregulated in these mice were host defense proteins such as BPI Fold Containing Family B Member 4 (Bpifb4), Cxcr4, and Dermokine (Dmkn), as well as *Aklr1c13* (Aldo–keto reductase family 1 member C13) and *Fndc9* (Fibronectin Type III Domain Containing 9) (Fig. 7a,b). Relative to *TG-Abi3-Gngt2*$^{+/+}$ mice, the molecular pathways represented by gene expression changes in *TG-Abi3-Gngt2*$^{-/-}$ mice include syncytium formation, cellular fusion, calcium mediated signaling, and extracellular matrix organization (Fig. 7c), recapitulating expected functional properties of the ABI family members [37]. Additional pathways that were enriched were gliogenesis (GO:0014015) and response to LPS (GO:0034189), consistent with altered glial homeostasis. We did not observe any significant gene expression changes in *TG-Abi3-Gngt2*$^{+/-}$ mice relative to *TG-Abi3-Gngt2*$^{+/+}$mice. In the *TG-Abi3-Gngt2*$^{-/-}$ mice, most of the gene expression changes were indicative of increased microglial ($p<0.05$ relative to *TG-Abi3-Gngt2*$^{+/-}$) and astrocytic involvement ($p<0.01$ relative to *TG-Abi3-Gngt2*$^{+/-}$; $p<0.05$ relative to *TG-Abi3-Gngt2*$^{+/+}$), with no changes observed in neuronal and oligodendrocyte-specific gene expression

(See figure on next page.)

Fig. 6 *Abi3-Gngt2* regulates gliosis in *APP* mice. Representative images of Iba-1 reactive microglia (**a**–**f**) and GFAP-reactive astrocyte (**g**-**l**) in 3-month-old or 6-month-old *APP* transgenic mice with WT (+/+), heterozygous (+/−), or KO (−/.−) of *Abi3-Gngt2* locus. Quantitation of the Iba-1 or GFAP staining from cortex or hippocampus is provided in corresponding panels on the right side. Scale bar, 50 μm. Clear symbols denote female mice and filled symbols denote male mice. $n=3$ females, 3 males (3 months) and $n=3$ females, 4 males (6 months). Data represents mean ± sem. One-way ANOVA; ***$p<0.001$; **$p<0.01$; *$p<0.05$

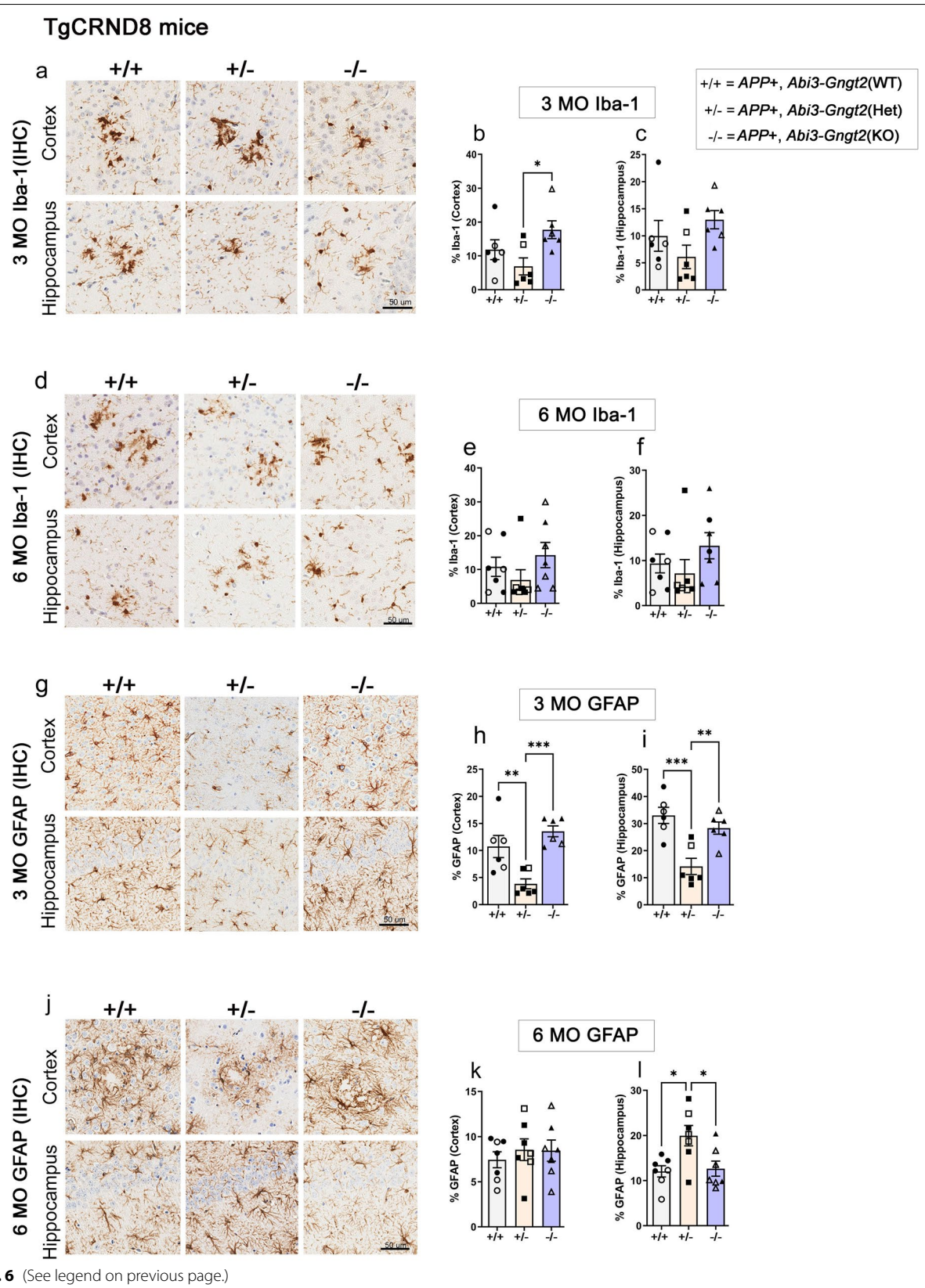

Fig. 6 (See legend on previous page.)

(Fig. 7d). Surprisingly, we found that in spite of reduced Aβ plaques, *TG-Abi3-Gngt2*$^{-/-}$ mice showed elevated gene signatures typically identified in AD tissues or preclinical models of AD. These mice showed upregulated PIG ($p<0.05$ relative to *TG-Abi3-Gngt2*$^{+/-}$; $p<0.05$ relative to *TG-Abi3-Gngt2*$^{+/+}$) [21], DAM ($p<0.05$ relative to *TG-Abi3-Gngt2*$^{+/-}$) [24], MGnD ($p<0.05$ relative to *TG-Abi3-Gngt2*$^{+/-}$) [25], and A1 astrocyte ($p<0.05$ relative to *TG-Abi3-Gngt2*$^{+/+}$) [38] gene profile signatures (Fig. 7e). We did not detect any selective induction of either the ARM [26] or A2 astrocyte [38] phenotypes in the three TG-*Abi3-Gngt2* genotypes (Fig. 7e). Notably, most of these modules (PIG, DAM, and MGnD) are driven by Apoe, Tyrobp, and Trem2 while the ARM signature is driven by specialized microglial subgroups overexpressing MHC II genes. WGCNA identified several gene co-expression modules that allowed us to correlate neuropathological traits to cell types (Fig. 7f), KEGG pathways (Additional File 10: Fig. S6a), module hub genes (Additional File 10: Fig. S6b-e), and glial signatures correlating with the modules (Additional File 10: Fig. S6f). Modules that were positively correlated with the *Abi3-Gngt2* genotype but were negatively correlated with Aβ biochemical levels or Aβ plaque burden included honeydew1 and plum3. These gene modules were primarily driven by microglia- and astrocyte-specific genes, respectively. We identified hub genes that regulate these different gene network modules (Additional File 10: Fig. S6b-e). Notably, Chil1/CHI3L1/YKL-40 (Chitinase-like 1) that is the top hub gene in honeydew1 is related to inflammation and AD pathophysiology [39]. The top hub gene in the plum3 module—Interferon Regulatory Factor 8 (Irf8)—corresponds to interferon signaling that has recently been identified to be upregulated in microglia from human AD [40]. This module is especially enriched for immune function, with the cd37 hub gene related to a Tyrobp-regulated microglial module in AD [41] and Lat2 identified as a core transcriptional signature of AD microglia [42]. Among these co-expression modules, we found that the plum3 module corresponds to homeostatic microglia signature (Additional File 10: Fig. S6c, f). Conversely, modules negatively correlated with the *Abi3-Gngt2* genotype but were positively correlated with Aβ biochemical levels or Aβ plaque burden was sienna3 which included a mixture of astrocyte and endothelial genes (Fig. 7d, Additional File 10: Fig. S6d). Overall, RNAseq and immunohistochemical data shows both amyloid-independent and amyloid-dependent immune signature in the *Abi3-Gngt2*$^{-/-}$ mice.

Exacerbated ptau accumulation in *Abi3Gngt2*$^{-/-}$ mice expressing human mutant tau

Because of the inherent dysfunctional immune milieu and early astrocytosis in the *Abi3-Gngt2*$^{-/-}$ mice, we decided to test how this would affect the development and progression of tauopathy. We used recombinant adeno-associated viruses (AAV) to deliver the pro-aggregant P301L/S320F mutant 0N/4R human tau, WT 0N/4R human tau, or a control vector in neonatal *Abi3-Gngt2*$^{-/-}$ mice or *Abi3-Gngt2*$^{+/+}$ mice [16, 43] (Fig. 8; Additional File 11: Fig. S7). We examined mice at 3 months of age and 6 months of age. We first confirmed that the expression of tau transgene was equivalent in P301L/S320F tau expressing *Abi3-Gngt2*$^{-/-}$ and *Abi3-Gngt2*$^{+/+}$ mice at 3 months (Fig. 8a,b) and 6 months (Fig. 8g,h). We did not find any human tau signal in the control vector-injected *Abi3-Gngt2*$^{-/-}$ mice or *Abi3-Gngt2*$^{+/+}$ mice as expected (Fig. 8a,b,g,h). We noticed that the level of phosphorylated tau (ptau) and misfolded pretangle tau was significantly higher in 3-month-old P301L/S320F tau expressing *Abi3-Gngt2*$^{-/-}$ mice compared to *Abi3-Gngt2*$^{+/+}$mice ($p<0.05$ for CP13 and MC1 respectively) (Fig. 8c–f). We also confirmed the presence of frank neurofibrillary tangles (NFT) in P301L/S320F tau expressing 3-month-old *Abi3-Gngt2*$^{-/-}$ and *Abi3-Gngt2*$^{+/+}$ mice by staining with ThioS (Additional File 11: Fig. S7a) or by biochemical analysis of insoluble tau following sequential extraction of cell lysates (Additional File 11: Fig. S7b-c). At 6 months of age, the P301L/

(See figure on next page.)

Fig. 7 Unbiased transcriptomic analysis of TG-*Abi3-Gngt2*$^{-/-}$ mice reveal distinctive disease-associated gene expression signatures and co-expression modules. **a**–**c** Volcano plot (**a**), list of top 5 upregulated and top 5 downregulated genes (based on fold change; orange, upregulated genes, blue, downregulated genes) (**b**) and GO pathways based on enriched genes for upregulated genes (**c**) in 3-month-old *APP* TG mice with WT (+/+), or KO (−/−) of *Abi3-Gngt2* locus. Orange dots, upregulated genes; blue dots, downregulated genes. FC, fold change; DEG, differentially expressed genes; padj, *p*-values adjusted for multiple comparison. **d** Cell type population analyses indicating changes in microglia, astrocytes, neurons, and oligodendrocyte populations in 3-month-old *APP* TG mice with WT (+/+), heterozygous (+/−), or KO (−/−) of *Abi3-Gngt2* locus. One-way ANOVA; $^{**}p<0.01$, $^{*}p<0.05$. **e** Gene expression signatures for specific microglia or astrocyte subtypes in 3-month-old *APP* TG mice with WT (+/+), heterozygous (+/−), or KO (−/.−) of *Abi3-Gngt2* locus. One-way ANOVA; $^{*}p<0.05$. **f** WGCNA gene co-expression modules correlating with experimental traits (biochemical Aβ values, plaque burden, Iba-1 burden, GFAP burden, *Abi3-Gngt2* genotype). Correlation of modules to different experimental traits is colored in a heatmap (red, positive correlation; blue, negative correlation). Modules with *p*-values < 0.05 and correlation value < -0.5 0r >0.5 are indicated in colored tile (see scale on right). Cell-type-specific gene lists were used to identify genes with significant overlap (odds ratio) within the modules. The heatmap is colored by the value of the odds ratio; higher the odds ratio of association, warmer the color. Grey squares indicate non-significant ($p > 0.05$, odds ratio < 2) overlaps in the gene lists. $N=4$ mice (2 males, 2 females) per *Abi3-Gngt2* genotype except 1 outlier removed in **d**, **e**. All *p*-values adjusted for multiple comparisons (padj)

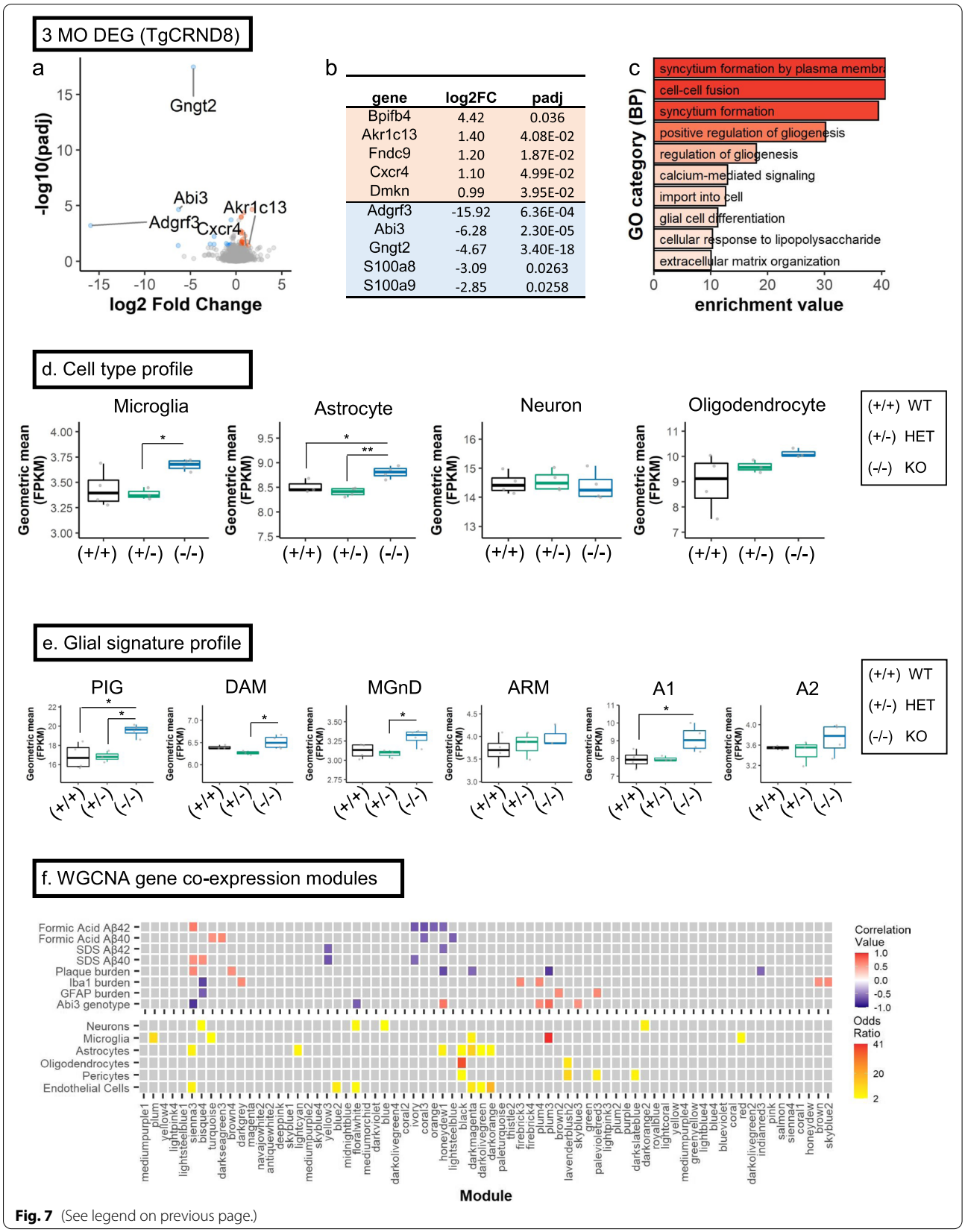

Fig. 7 (See legend on previous page.)

S320F tau expressing *Abi3-Gngt2*$^{-/-}$ mice showed higher ptau immunoreactivity compared to *Abi3-Gngt2*$^{+/+}$ mice (Fig. 8i,j; $p < 0.001$), while the levels of pretangle tau were equivalent between the two groups (Fig. 8k,l). None of the control-injected mice showed any detectable ptau or misfolded tau at either age (Fig. 8c–f, i–l).

We also examined the neuropathologies in human WT tau expressing *Abi3-Gngt2*$^{-/-}$ mice and *Abi3-Gngt2*$^{+/+}$ mice. In the 3-month-old cohorts, we did not find any differences in the total tau levels or ptau levels of *Abi3-Gngt2*$^{-/-}$ and *Abi3-Gngt2*$^{+/+}$ mice (Additional File 11: Fig. S7d-g), nor did we see any induction of MC1-reactive pretangle tau (data not shown). In the 6-month-old cohort, while the levels of tau expression were comparable (Additional File 11: Fig. S7l-m), we noticed higher ptau levels in *Abi3-Gngt2*$^{-/-}$ mice relative to *Abi3-Gngt2*$^{+/+}$ mice ($p < 0.0001$) (Additional File 11: Fig. S7n-o). Overall, our data indicates that early astrocytosis accompanying loss of *Abi3-Gngt2* resulted in increased ptau in two separate tau cohorts.

Robust astrocytosis induced by tau overexpression in *Abi3-Gngt2*$^{-/-}$ mice

We wanted to examine whether the inherent immune phenotype in *Abi3-Gngt2*$^{-/-}$ mice would be exacerbated in the presence of ptau (Fig. 9). In 3-month-old mice, P301L/S320F tau expression had a robust microglial response in the *Abi3-Gngt2*$^{+/+}$ mice ($p < 0.01$ relative to control vector; $p < 0.05$ relative to tau expressing *Abi3-Gngt2*$^{-/-}$ mice) (Fig. 9a,b). At 6 months of age, the P301L/S320F tau expressing *Abi3-Gngt2*$^{-/-}$ mice showed higher microglial response than the rest of the cohorts ($p < 0.01$ relative to control vector) (Fig. 9c,d). Notably, Iba-1-reactive microglia in the control vector injected *Abi3-Gngt2*$^{-/-}$ mice was comparable (6 months) or lower than (3 months) P301L/S320F tau expressing WT *Abi3-Gngt2*$^{+/+}$ mice. In WT tau expressing mice, we observed similar age-dependent pattern for microgliosis where tau expression increased microglial response in *Abi3-Gngt2*$^{-/-}$ mice at 6 months of age (Additional File 11: Fig. S7j, k, r, s).

In the 3-month-old and 6-month-old P301L/S320F tau expressing *Abi3-Gngt2*$^{-/-}$ mice, we observed higher astrocytosis concordant with increased pathological tau accumulation (Fig. 9e–h). P301L/S320F tau expressing *Abi3-Gngt2*$^{-/-}$ showed higher GFAP burden relative to control vector ($p < 0.0001$) as well as P301L/S320F tau expressing *Abi3-Gngt2*$^{+/+}$ mice ($p < 0.001$) at both ages. Thus, the astrocytic response to tau was more consistent with the neuropathology at both ages. This data also reveals an interesting dichotomy in the response of astrocytes and microglia to pathological tau, especially at the younger age examined (Fig. 9b vs f).

In 3-month-old WT tau expressing mice, astrocytosis immunoreactivity was more enhanced in *Abi3-Gngt2*$^{+/+}$ mice than *Abi3-Gngt2*$^{-/-}$ mice ($p < 0.05$) (Additional File 11: Fig. S7h-i). At 6 months of age, however, we observed higher levels of astrocytosis in WT tau expressing *Abi3-Gngt2*$^{-/-}$ mice compared to *Abi3-Gngt2*$^{+/+}$ mice (Additional File 11: Fig. S7p-q; $p < 0.01$). This implies an age-dependent as well as neuropathology-dependent immune phenotype induced by WT tau overexpression in the *Abi3-Gngt2*$^{-/-}$ mice, similar to what was observed for Iba-1 microgliosis ((Additional File 11: Fig. S7r-s). Overall, the effect of tauopathy on astrogliosis was most prominent in 6-month-old *Abi3-Gngt2*$^{-/-}$ mice.

AD-associated mutation alters ABI3 phosphorylation

To understand the differences between WT ABI3 and AD-associated S209F mutant ABI3, we overexpressed the corresponding C terminal FLAG-tagged recombinant constructs in HEK293T cells. C terminally FLAG-tagged ABI3 has been previously shown to be functionally active [44]. We detected ABI3 protein using either anti-FLAG antibody, an in-house antibody raised against S209 ABI3 or a commercially available N terminal-specific ABI3 antibody (Millipore Sigma). We observed that wild type ABI3, but not S209F ABI3 migrated as a double band (Fig. 10a) which is consistent with data reported earlier [44]. To confirm that the band migrating on the top is a phosphorylated form, we incubated WT ABI3 or S209F ABI3 transfected HEK293T cell lysates with Lambda Protein Phosphatase. Incubation with Lambda Protein Phosphatase at 30 °C, but not at 4 °C, abolished the upper band in WT ABI3 lysate (Fig. 10b). Mutating the phenylalanine (F) at position 209 to dephospho-mimetic alanine (A) or phospho-mimetic aspartate (D) reverses this deficit in phosphorylation to levels that are comparable to WT ABI3 protein (Fig. 10c,d). This shows that presence

(See figure on next page.)

Fig. 8 *Abi3-Gngt2* deficiency accelerates tauopathy in a mutant human tau model. *Abi3-Gngt2*$^{+/+}$ (WT) and *Abi3-Gngt2*$^{-/-}$ (KO) mice were injected with control vector (Control) or AAV expressing a double mutant (P301L/S320F) human 0N/4R tau in the cerebral ventricles on neonatal day P0 and analyzed at 3 months (**a**–**f**) or 6 months (**g**–**l**) of age. Representative brain images indicating total human tau (detected with CP27 antibody, **a**, **g**), ptau (detected with CP13 antibody, **c**, **i**), and misfolded pretangle tau (detected with MC1 antibody, **e**, **k**) from cortex and hippocampus are shown. Quantitative analysis from both cortex and hippocampus of antibody-stained slides (**b**, **d**, **f**, **h**, **j**, **l**) shown on right side of corresponding stained brain images (**a**, **c**, **e**, **g**, **i**, **k**). Scale bar, 75 µm. $n = 6$ mice/group. Data represents mean ± sem. One-way ANOVA; ****$p < 0.0001$; ***$p < 0.001$; **$p < 0.01$; *$p < 0.05$

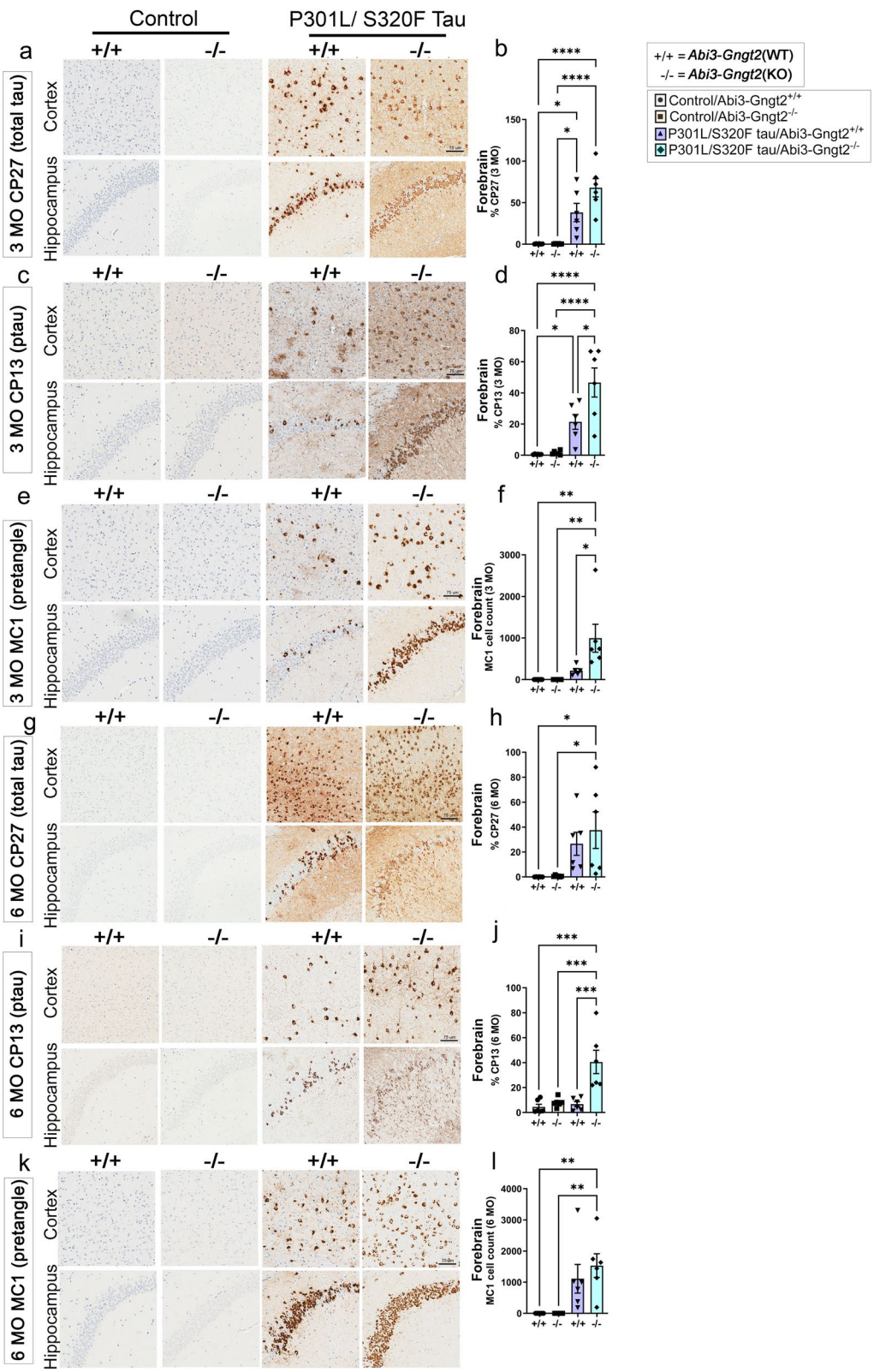

Fig. 8 (See legend on previous page.)

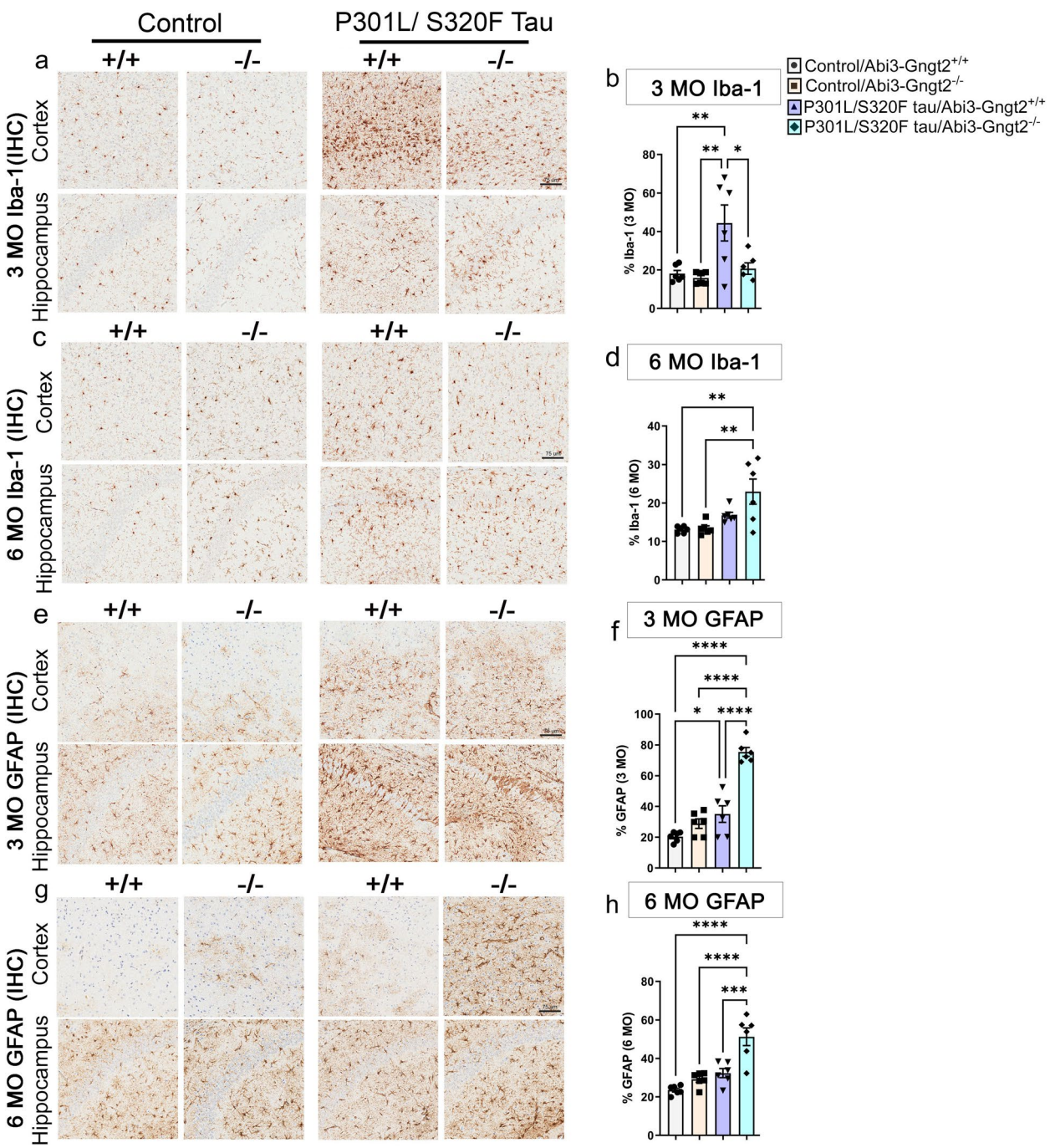

Fig. 9 Increased astrocytosis in tau expressing *Abi3-Gngt2*$^{-/-}$ mice. *Abi3-Gngt2*$^{+/+}$ (WT) and *Abi3-Gngt2*$^{-/-}$ (KO) mice were injected with control vector (Control) or AAV expressing a double mutant (P301L/S320F) human 0N/4R tau in the cerebral ventricles on neonatal day P0 and analyzed at 3 months or 6 months of age. Representative images of Iba-1 reactive microglia (**a**–**d**) and GFAP-reactive astrocyte (**e**–**h**) in 3-month-old or 6-month-old mice are shown. Quantitation of the Iba-1 or GFAP staining from forebrain (cortex and hippocampus) is provided in corresponding panels on the right side. $N = 6$ mice/group. Scale bar, 75 µm. Data represents mean ± sem. One-way ANOVA; ****$p < 0.0001$; ***$p < 0.001$; **$p < 0.01$; *$p < 0.05$

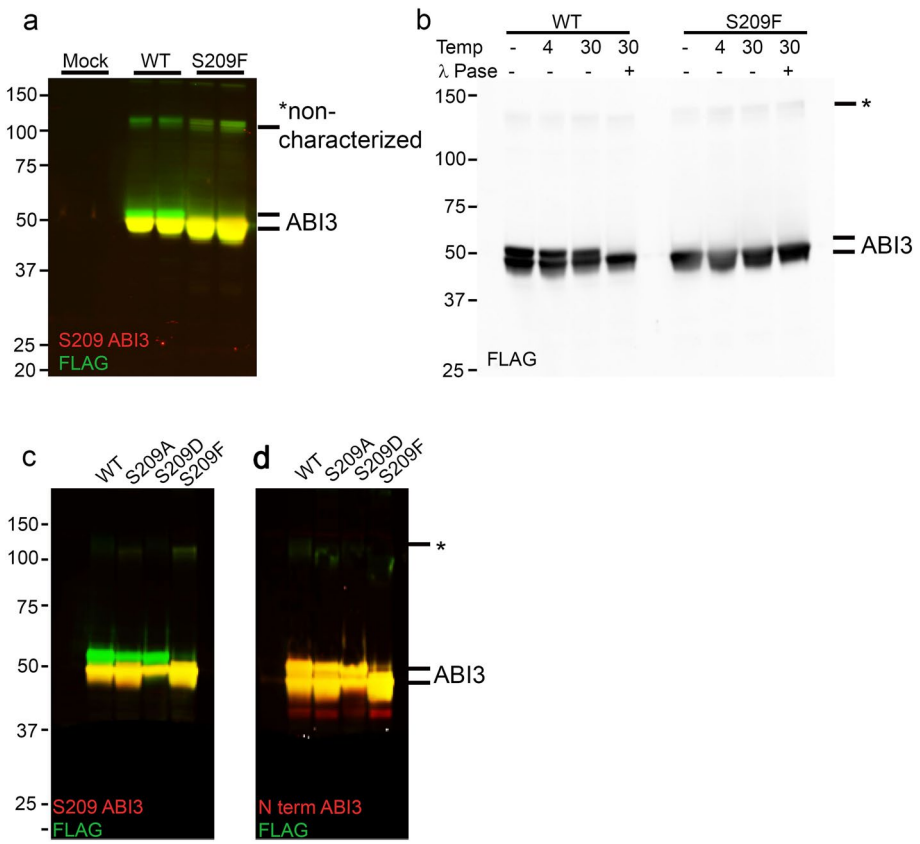

Fig. 10 S209F mutation leads to altered phosphorylation in ABI3 protein. **a** HEK293T cells were transiently transfected with WT ABI3 or S209F ABI3 and separated on an immunoblot showing two distinct bands around 50 kDa. Higher bands that are as yet uncharacterized (marked by asterisk) are also denoted. The proteins were detected with two antibodies simultaneously using LiCor infrared dyes: anti-FLAG antibody (green) and anti S209-ABI3 antibody (red). **b** Lambda protein phosphatase assay performed at 30 °C on WT ABI3 and S209F ABI3 expressing HEK293T cell lysates detected with anti-FLAG antibody. **c**, **d** HEK293T cells were transiently transfected with WT ABI3 or ABI3 mutated at position 209 and separated on an immunoblot. The proteins were detected with two antibodies simultaneously using LiCor infrared dyes: anti-FLAG antibody (green) and anti S209-ABI3 antibody (red) (**c**) or anti-FLAG antibody (green) and anti N terminal ABI3 (Sigma) (red) (**d**). "Mock" denotes sham transfection procedure with no DNA. Data representative of at least two independent experimental replicates

of phenylalanine at position 209 specifically impairs overall ABI3 phosphorylation, though auto-phosphorylation at this site is not necessary. Since, phosphorylation of Abi family of proteins is related to their stability and function [45], this would imply that the Ser to Phe mutation could render the ABI3 protein functionally inactive.

Discussion

The mechanism through which ABI3 alters risk for AD remains uncertain. Here we document that Abi3, though primarily expressed in microglia, is also expressed in other cells in humans and *APP* transgenic mice brain, showing age-associated increases in its transcript levels. Characterization of an *Abi3*$^{-/-}$ mouse strain identified that the overlapping gene *Gngt2* is also knocked out. We conducted additional analyses to demonstrate that *Abi3* and *Gngt2* expression are tightly co-regulated in both mice and humans, suggesting some form of functional synergy. Using this *Abi3-Gngt2*$^{-/-}$ mice, we show that loss of Abi3-Gngt2 expression predisposes the mice to an immune phenotype characterized by reactive gliosis and gene expression patterns resembling an AD-associated profile. Notably in these mice, the AD/neurodegeneration-associated genes Trem2, Plcg2, Tyrobp, and Csf1r are upregulated in a gene dose-dependent manner, even in the absence of Aβ. We also find that the loss of *Abi3-Gngt2* locus has opposing effects on amyloid and tau pathology in mice (Fig. 11a,b). Loss of this locus results in a reduction in amyloid pathology and preservation of synaptic markers, though effects on amyloid are diminished as the mice age. In contrast, we noted that loss of *Abi3-Gngt2* markedly increases tau pathology. Because Abi3 is expressed in neurons as well as microglia, it is

a

Mouse Cohort (*Abi3-Gngt2-/-*)	Aβ plaque	ptau burden	Pretangle burden
CRND8 (3 month)	↓	n.d.	n.d.
CRND8 (6 month)	↓	n.d.	n.d.
AAV-P301L/S320F tau (3 month)	n.d.	↑	↑
AAV-P301L/S320F tau (6 month)	n.d.	↑	↔
AAV-WT tau (3 month)	n.d.	↔	n.d.
AAV-WT tau (6 month)	n.d.	↑	n.d.

b

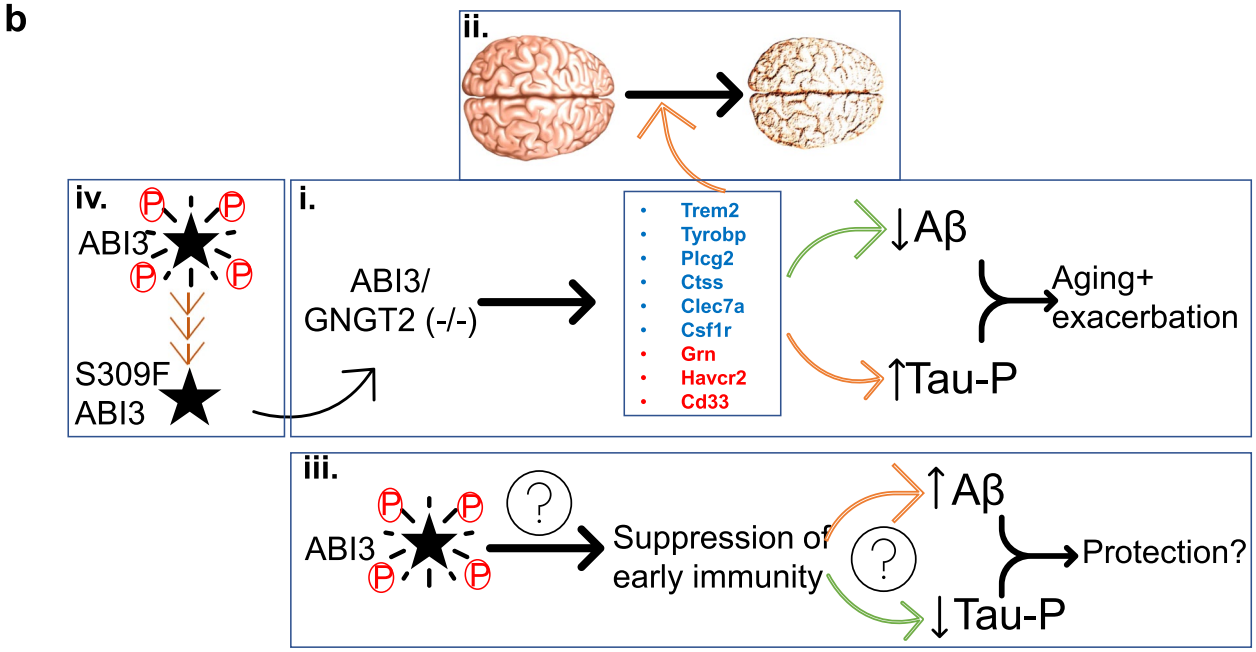

Fig. 11 Hypothetical scenarios linking Abi3-Gngt2 function to AD. **a** Tabulated view of neuropathological findings in *Abi3-Gngt2*$^{-/-}$ mice relative to *Abi3-Gngt2*$^{+/+}$ mice. n.d., not done. **b** Schematic summary of possible Abi3/Gngt2 function in the context of AD. Our experiments with *Abi3-Gngt2* deficient model show that immune phenotype in these mice reduce Aβ plaques in a gene dose- and age-dependent manner in TgCRND8 mice but increase tau phosphorylation in AAV-tau model (i). Loss of Abi3-Gngt2 function leads to early-life induction of AD/amyloid-associated factors and microglial genetic risk factors, independent of Aβ. In fact, these same microglial factors (as tabulated in i) are altered as humans progress from healthy status to AD (ii). Based on our data, we hypothesize that a normally functioning Abi3 would lead to suppression of immunity (by suppressing induction of AD disease microglial risk factor genes), thus increasing Aβ plaques but preventing tau phosphorylation and tangle formation (iii). Whether this would modulate synaptic resilience and dementia progression resulting in protective effects requires further investigation. The neuropathology in the *Abi3-Gngt2* deficient model is reminiscent of the dichotomy observed in multiple AD mouse models. The differential response of Aβ and tau to immune activation necessitates a cautious foray into immune-targeted therapies. Future work in rodent models of Aβ deposition and tau pathology in the presence of the S209F mutated Abi3 would provide critical functional information. Our in vitro data shows that the AD associated S209F mutation dramatically reduces self-phosphorylation, which guided by previous data from ABI family of proteins, would imply a loss of function phenotype (iv). Brain picture (ii) adapted from online source under CC license

possible that the effect of *Abi3-Gngt2* on Aβ and tau could be modulated by glial as well as neuronal signaling pathways. Our experimental models, whereby we observed functional dichotomy in Abi3-mediated immunoproteostasis in Aβ and tau models, allow us to impute the probable function of the *ABI3* risk variant in influencing AD risk. If, for example, the detrimental effect of S209F Abi3 is mediated by increasing Aβ,

then the disease-associated mutation is expected to reinforce additional functional characteristics. On the other hand, if the effect is cell autonomous, leading to deregulation of microglial surveillance activity [46, 47] or exacerbating neuronal tauopathy, then the mutation could be mimicking a loss of function phenotype. Indeed, examples of such context-dependent manifestations can be found in Trem2 models, where depending on the disease stage, neuropathology, and gene dosage, Trem2 expression (or lack of) recapitulates a partial loss-function or demonstrates additional pathological characteristics [48–51]. Taken together, our data show that a dysfunctional immune environment accompanying the lack of *Abi3-Gngt2* is associated with a dichotomous effect on Aβ and tau proteinopathy.

A recent study, using a bigenic model of 5xFAD and *Abi3-Gngt2*$^{-/-}$ mice, reported increased Aβ plaques at 8 months of age and an inflammatory gene expression signature similar to our data [47]. However, this report could not specifically attribute the DAM profile to *Abi3-Gngt2* genotype [47]. While the changes in Aβ proteinopathy is opposite of what we have observed, this could be due to this study using a single time point in older mice and a mouse model expressing both mutant *APP* and *PS1* genes. Whether *Abi3-Gngt2* could have an additional interaction with PS1-related phenotype remains to be studied. Notably, other studies have reported disparate observations in genetically identical mouse models of neurodegenerative proteinopathies, especially those that undergo immune manipulations. A recent example is when the profound systemic and neural inflammation inherent in the c9orf72-deficient mice was found to be reversed when maintained in a different mouse facility [52]. In fact, immune-related phenotypes, as inherent in this *Abi3-Gngt2*$^{-/-}$ mice, are extremely sensitive to environmental factors and local immune stressors that can regulate metabolic homeostasis and modulate CNS health [53].

Our study highlights the utility of detailed transcriptomic analysis in phenotyping new disease models. During our study, we found that the *Gngt2* gene, whose putative promoter region and a non-coding exon of one transcript isoform overlaps with the *Abi3* locus, is also lost in this velocigene knockout model. *Gngt2* is reported to be a microglia-specific gene and is involved in cone phototransduction [54]. To establish the physiological relevance of this dual knockout, we used extensive informatics analysis from human and mice showing that *ABI3* and *GNGT2* are co-regulated, indicating that these two genes exist in a co-expression network. While the original exome analysis data [6] did not find any AD risk related to *GNGT2*, a newer study identified *GNGT2* as one of the 989 genes that mapped to the 38 genomic loci related to AD risk [8]. Future studies should dissect out the specific functions of these two genes resident in the *ABI3* locus.

Our study is an exemplar for highlighting how immune function can be differentially related to development and progression of amyloid and tau pathologies that occur concurrently in the brain. Indeed, manipulation of expression of Trem2, Tyrobp, Cx3cl1/Cx3cr1, IL1β, and IFN-γ have all been shown to have opposing effects on amyloid and tau pathologies [49–51, 55–65]. Hippocampal expression of IL-1β was shown to robustly reduce plaques in the APP/PS1 model and 3xTg-AD model but worsened tauopathy in the 3xTg-AD model [62, 63]. Similarly, deficiency of Cx3cr1 reduced amyloid deposition in two different *APP* models but aggravated tau hyperphosphorylation in hTau mice [65, 66]. More recently, this dichotomy has been elegantly demonstrated in multiple models of Trem2 and Tyrobp [49–51, 55–59]. The outcomes of *Abi3-Gngt2* deletion on amyloid pathology was determined by age as also gene dose, which is consistent with studies on Trem2 models of AD [49, 57]. Altogether, this indicates that immune function can have distinctive effects on Aβ and tau, a paradigm that we have referred to as immunoproteostasis [2]. Immunoproteostasis outcomes are also expected to be modified by the disease stage or the strength of the immune signal. Studies in human patients support this notion of a dichotomous role of inflammation, where data indicates that early inflammation may play a protective role in prodromal AD phase and in monkeys [67–69] but that chronic age-associated inflammation may be overwhelmingly detrimental. How this immunoproteostasis additionally ties to synaptic resilience and neurodegeneration in the presence of multiple proteinopathies as observed in AD [70], remains to be characterized. Harnessing the immune system as a potential treatment for AD is attractive [2]. Our current data, however, highlights the challenges of harnessing immunoproteostasis to treat AD as such therapies could theoretically have opposing effects of amyloid and tau pathologies and exacerbate underlying synaptic functions through independent mechanisms. Thus, designing immune-based therapies warrants cautious deliberation with careful consideration of disease stage and immune mediator function.

Understanding how immunoproteostasis is modified by brain neuropathology and age is important as this is expected to modify the efficacy of immune-based therapies. For amyloid pathology, there is data that activated micro/astroglia enhances Aβ phagocytosis [60, 62, 71], which is a desired outcome, but why that glial activation state appears to be associated with enhanced tau pathology remains enigmatic. Given that large number of immune signaling pathways are altered in our current

study and in previous studies on AD immunoproteostasis [2], it will be challenging to gain more detailed mechanistic insights into the function of Abi3 vis-à-vis AD cascade. Indeed, it may not be a single pathway or factor that results in these age- and pathology-related dichotomous outcomes but the combined action of many different signaling alterations on Aβ and tau metabolism. Given that alterations in immune signaling induced by amyloid deposition are a clear hallmark of AD, such data provide alternative, but not mutually exclusive, mechanisms for spreading of tau pathology. Indeed, signaling initiated by microglia or astrocytes in response to amyloid deposition could then trigger induction of tau pathology. Such signaling could explain the apparent crosstalk between amyloid and tau [72], characterized by the unique region-specific spread of tau and could explain the temporal lag between amyloid deposition and tau tangle formation in humans subsequently leading to loss of synaptic plasticity and initiation of cognitive decline [70].

Analysis of co-expression networks reveals interesting transcriptomic differences in parental *Abi3-Gngt2*$^{-/-}$ lines and the TG-*Abi3-Gngt2*$^{-/-}$ lines. While the parental *Abi3-Gngt2*$^{-/-}$ lines mostly indicated an abundance of immune signature, the TG-*Abi3-Gngt2*$^{-/-}$ mice showed additional signatures consistent with the known functions of the ABI family of proteins [37]. Consideration of these functions—calcium mobilization, extracellular matrix reorganization, and intercellular communication [73]—will be important in understanding AD cascade in addition to the involvement of more well-characterized phagocytotic and debris removal functions of microglia. Indeed, a recent study suggests that Abi3-Gngt2$^{-/-}$ microglia exhibits reduced surveillance of brain parenchyma [46]. In terms of the hub genes identified in our study, Chi3l1/YKL-40 is singularly important as it is correlated with the *Abi3-Gngt2* genotype in our study. YKL-40 is primarily an astrocytic protein that is elevated in AD and is considered a potential biomarker [74]. Recently YKL-40 has been shown to have non-cell autonomous activity in the brain, affecting microglial function, circadian clock, and generally AD progression [75]. Whether Abi3 plays a role in AD neuropathologic cascade by modulating YKL-40 function remains an untested possibility.

ABI3 has been imputed to be of microglial origin [42]. A previous study has reported clusters of ABI3-positive microglia localized around Aβ deposits in AD patients [11]. Our in situ hybridization data indicates that ABI3 is present in both microglia and neurons. We also show that the amount of ABI3 transcript levels increases in concordance with increasing Aβ deposits. Because Abi3 is present in both neurons and microglia, its role in non-cell autonomous and cell autonomous signaling in AD proteinopathy and disease progression could be equally important. Our unexpected finding of neuronal ABI3 is reminiscent of the observations on PLCG2, which was initially thought to be myeloid cell-specific, but its RNA was also found in neurons and endothelial cells [76]. *PLCG2*, like *ABI3*, was identified as an AD protective factor using exome analysis strategies [6]. Given that protein levels in any specific cell cannot always be inferred from RNA levels [77], some caution is warranted here before our in situ observations can be confirmed by protein detection methods.

The ABI family of proteins, especially ABI-1 and ABI-2, are involved in cytoskeletal reorganization [37]. The function of ABI3, much less S209F ABI3, in the brain is unknown. Some previous studies have reported ABI3 in microglia with ramified or amoeboid morphology [11, 42]. Another recent paper showed that absence of *Abi3* (using the same models as used in this study) alters microglial morphology and curbs its function in homeostatic surveillance [46, 47]. This would be consistent with the previously documented role of ABI3 in regulating cytoskeletal dynamics [10, 78]. Our RNAseq data also illuminates inherent differences in neuronal and glial populations in mice completely deficient in *Abi3-Gngt2*, even in the absence of Aβ. Indeed, these mice show upregulated PIG profile that is related to a variety of cellular functions involving multiple cell types, such as complement cascade, neuronal auto-lysosomal pathways, antigen processing and presentation, oxidation–reduction, and inflammatory gliosis. Originally, the PIG profile was found to be concordant with high Aβ burden, independent of tau, and also overlapping with co-expression network changes identified in ALS [21]. This suggests that these *Abi3-Gngt2* KO mice have an underlying neurodevelopmental phenotype, mimicking some of the early changes observed in aging brains.

The *Abi3-Gngt2*$^{-/-}$ mice also show increased Trem2, Tyrobp, and Plcg2, which would be consistent with cooperativity between different AD-associated risk factors. In fact, we observed this early immune activation in the absence of Aβ, which could illuminate how underlying genetic risk factors could crosstalk to prime the aging brain, even before the frank appearance of proteinopathy. Crosstalk between AD risk immune genes has been recently demonstrated, notably between Cd33 and Trem2 [79]. The TG-*Abi3-Gngt2*$^{-/-}$ mice also, over time, showed dysfunctional immune phenotype, with age-dependent reduction of beneficial effect on Aβ and accumulation of ptau. Overall, this would suggest that loss of *Abi3-Gngt2* function leads to early induction of immunity that could lead to detrimental outcomes in the longer term (Fig. 11). It is known that phosphorylation is key to maintaining the stability and function of ABI

family of proteins [37, 80]. Thus, our data suggests that the AD-associated mutation could result in hypomorphic function or partial loss of function. Based on our data, it is tempting to suggest that wild type ABI3 could suppress immune gene expression and modulate the cross-talk between different AD immune risk factors that is normally associated AD progression and possibly lead to more balanced neuro-immune homeostasis (Fig. 11).

Limitations

Although our study establishes an important paradigm in neuro-glial interactions in AD neuropathology, a limitation of our study is that the locus deletion in the mice used in this study affected two genes that have overlapping sequences. In addition, gene deletion studies may also miss subtle physiological insights when such genes have complex disease-stage- or age-dependent outcomes, such as having both gain and loss of function phenotype with respect to different aspects of brain homeostasis. While our data suggests that AD-associated Abi3 mutation could possibly act as a loss of function variant, this premise would need to be validated in experimental models carrying this particular AD-associated variant. Another limitation is we have inferred the effect of *Abi3-Gngt2* deletion on Aβ and tau using independent, stand-alone models and thus, how this could affect AD phenotype, which is characterized by combinatorial Aβ and tau pathologies, still needs to be characterized.

Conclusions

Overall, our data points to immune functions playing dichotomous roles in influencing AD-related neuropathologies. This warrants careful consideration of therapies targeting the immune system.

Abbreviations

+/+: Wild type for *Abi3-Gngt2*; +/−: Haploinsufficiency of *Abi3-Gngt2* (heterozygous); −/−: Complete deficiency of *Abi3-Gngt2* (knockout); AAV : Adeno-associated virus; Aβ : Amyloid β; ABI3: Abelson Interactor Protein 3; AD: Alzheimer's disease; Adamts6: ADAM Metallopeptidase With Thrombospondin Type 1 Motif 6; Adgrf3: Adhesion G Protein-Coupled Receptor F3; Aklr1c13: Aldo-keto reductase family 1 member C13; AMP-AD: Accelerating Medicines Program for Alzheimer's disease; ARM: Activated response microglia; CER: Cerebellum; Chil1: Chitinase-like 1; Clec7a: C-type lectin domain family 7 member A; Cxcr4: C-X-C Motif Chemokine Receptor 4; DAM: Damage associated microglia; DEG: Differentially expressed genes; DLPFC: Dorsolateral prefrontal cortex; Dmkn: Dermokine; FA: Formic Acid; FC: Fold change; Fndc9: Fibronectin Type III Domain Containing 9; FPKM: Fragments per kilobase of exon per million mapped fragments; GO: Gene Ontology; GFAP: Glial fibrillary acidic protein; Gngt2: Guanine Nucleotide Binding Protein Gamma Transducing Activity Polypeptide 2; GS: Gene significance value to specific experimental trait; Het: Heterozygous; Iba-1: Ionized calcium-binding adapter molecule 1; Irf8: Interferon Regulatory Factor 8; Ly86: Lymphocyte Antigen 86; kWithin: Extent of gene connectivity within the module; MAF: Minor allele frequency; MM: Module membership value; MGnD: Microglial neurodegenerative phenotype; Mpeg1: Macrophage Expressed 1; MAPT: Microtubule associated protein tau; Nramp1: Natural resistance-associated macrophage protein 1; NESH: New molecule including SH3; NFT: Neurofibrillary tangles; nonTG: Nontransgenic for *APP*swe/ind (CRND8 line); ns: Non-significant; Olfml3: Olfactomedin-Like 3; OR: Odds ratio; padj: *p*-Values adjusted for multiple comparisons; Pcdha5: Protocadherin Gamma Subfamily A 5; PIG: Plaque-induced genes; QC: Quality control; RNA sequencing: RNAseq; S100a9: S100 Calcium-Binding Protein A9; SDS: Sodium dodecyl sulfate; SH3: Src homology 3; Slc11a1: Solute Carrier Family 11, Member 1; Sval1: Seminal vesicle antigen-like 1; TCX: Temporal cortex; ThioS: Thioflavin S; TG: Transgenic for *APP*swe/ind (CRND8 line); Tnfrsf1b: Tumor Necrosis Factor Receptor Superfamily, Member 1B; WGCNA: Weighted gene co-expression network analysis; WT: Wild type.

Supplementary Information

The online version contains supplementary material available at https://doi.org/10.1186/s13195-022-01044-1.

Additional file 1: Table S1. Description of resources and reagents used in this study.

Additional file 2: Table S2. Normalized RNA levels (FKPM values) of Abi3 and Gngt2 from TgCRND8 mice at various ages.

Additional file 3: Table S3. Normalized RNA levels (FKPM values) of Abi3 and Gngt2 from rTg4510 mice at various ages.

Additional file 4: Fig. S1. Cellular localization of ABI3 RNA in human and mouse. In situ hybridization was done to detect Abi3 RNA on human (a-f) and mouse (g-x) paraffin embedded brain sections. Human or mouse ABI3 specific RNAscope probes were used for in situ hybridization detected by Fast Red (red color) followed by immunohistochemistry for Iba-1 antibody detected by DAB (brown color). Representative forebrain images are shown. Asterisks mark Aβ deposits; arrowheads indicate Iba-1 (microglia) associated in situ signal and arrows indicate in situ signal in non-microglia cells. It should be noted that the presence of amyloid deposits is imputed from the focal clustering of microglia and cellular morphology, in the absence of amyloid staining. *n*=3 (human AD cases, 6 month old TG-*Abi3-Gngt2*$^{-/-}$ mice and 6 month old TG-*Abi3-Gngt2*$^{+/+}$ mice mice) and *n*=1 (18 month old TgCRND8 mice, collected independent of this study). Representative of two independent experimental replicates. Please note that this figure also contains the images depicted in Fig 1c-f. TG= transgenic CRND8. Also see Fig. 1.

Additional file 5: Fig. S2. Genomic organization at the *Abi3* locus of Mus musculus. a. RNAseq based confirmation of Abi3, Gngt2 and APP levels from three *Abi3* genotypes in *APP* transgenic (*APP*, Tg) mice or nontransgenic (*APP*, nTg) mice. *Abi3*, WT: *Abi3*$^{+/+}$; *Abi3*, het: *Abi3*$^{+/-}$; *Abi3*, hom: *Abi3*$^{-/-}$. x axis denotes the genotypes and y axis denotes FPKM values of the corresponding RNA indicated on top of the graph. *N*=4 mice/genotype. b. The *Abi3* knockout mice (Abi3tm1.1(KOMP)Vlcg) was generated by cre-mediated excision of the parental Abi3tm1(KOMP)Vlcg allele resulting in the removal of the neomycin selection cassette, leaving behind the inserted lacZ reporter sequence. The sequence that was excised out on chromosome 11 was located between 95842143 and 95832627 (indicated by black bar). This fragment encompasses the *Abi3* coding region and 5' region of a *Gngt2* isoform.

Additional file 6: Table S4. Analysis of *Abi3* and *Gngt2* expression changes in mouse studies (transcriptomic data originally reported by Wan et al. [33] and Al Ouran et al [34] and available at http://mmad.nrihub.org).

Additional file 7: Fig. S3. Hub genes from WGCNA modules identified in 3 month old *Abi3-Gngt2*$^{-/-}$ mice. a. Volcano plot and table of altered genes representing DEG in 3 month old heterozygous *Abi3-Gngt2*$^{+/-}$vs WT *Abi3-Gngt2*$^{+/+}$mice. FC, fold change; padj, adjusted *p*value. b-d. WGCNA module membership is plotted against gene connectivity (kWithin) for genes identified within modules significantly correlated with *Abi3-Gngt2* genotype and glial burden traits in *Abi3-Gngt2*$^{-/-}$mice. Accompanying table shows top hub genes (as ranked by kWithin values) identified in each co-expression WGCNA modules of 3 month old *Abi3-Gngt2*$^{-/-}$mice relative to *Abi3-Gngt2*$^{+/+}$ mice. The module members of antiquewhite2, coral2 and mediumpurple2 modules are shown. Module statistics are denoted by: kWithin, extent of gene connectivity within the module; MM, module membership value (of gene to module); GS, gene

significance value to specific experimental trait. e. The overlap of genes within WGCNA modules with genes previously identified in AD-associated microglial and astrocytic subtypes is expressed as odds ratio value. The different cell signatures are: neurotoxic A1 and neurotrophic A2 astrocyte [38]; PIG network [21]; DAM [25]; MGnD and homeostatic microglia [24]. Higher odds ratio (warmer color) denotes higher correlation. All p values are adjusted for multiple testing. Grey boxes indicate non-significant odds ratio values. f. Genes within WGCNA modules associated with known KEGG pathways based on over-representation of enriched genes in *Abi3-Gngt2*$^{-/-}$mice (relative to *Abi3-Gngt2*$^{+/+}$) is depicted in a bubble plot. Pathways with an over-represented p-value ≤ 0.05, the number of module genes within the pathway >5 and an enrichment score >1.5 are depicted. The bubble plot is colored by p-value (blue color; higher p value is indicated by deeper blue hues) and sized by the enrichment score (circle diameter). *N*=4 mice (2 male, 2 female) per cohort.

Additional file 8: Fig. S4. Neuropathological attributes of TG-*Abi3-Gngt2*$^{-/-}$ mice. a-b. Anti CT20 immunoblot indicating full length APP and C terminal fragments (CTF) in *APP* transgenic mice with WT (+/+), heterozygous (+/−) or KO (−/−) of *Abi3-Gngt2* locus (a). Lane marked with asterisk denotes a nonTg mice for *APP* genotype (a). APP levels normalized to actin is depicted (b). *n*=3-4 mice/group. Ubiquitin decorating Aβ plaques in 3 month (c) and 6 month old (d) *APP* TG mice with WT (+/+), heterozygous (+/−) or KO (−/−) of *Abi3-Gngt2* locus. Scale Bar, 2mm (whole brain), 50 µm (cortex and hippocampus). e-m. Representative brain images stained with 33.1.1 antibody and corresponding quantitation (e-f), GFAP antibody and corresponding quantitation (g-h), Iba-1 antibody and corresponding quantitation (i-j), cd11b and corresponding quantitation (k-l) and ubiquitin decorated Aβ plaques (m) in 9 month old *APP* TG mice with WT (+/+) or heterozygous (+/−) *Abi3-Gngt2* locus. Scale Bar, 2 mm (whole brain), 50 µm (cortex and hippocampus). *N*=7-8 mice/genotype. Data represents mean±sem. Clear symbols denote female mice and filled symbols denote male mice.

Additional file 9: Fig. S5. Synaptic protein levels in TG-*Abi3-Gngt2*$^{-/-}$ mice. Immunoblotting depicting levels of synaptic proteins in 3 month old *APP* Tg mice with WT (+/+), heterozygous (+/−) or KO (-/-) of *Abi3-Gngt2* genes (a, c, e, g, i, k, m). Quantitation of the synaptic proteins normalized to actin or GAPDH is depicted (b, d, f, h, j, l, n). Molecular weight markers in kDa are indicated on each panel. *N*=4 mice/genotype. Data represents mean±sem. 1-way Anova; ***p*<0.01; **p*<0.05.

Additional file 10: Fig. S6. Hub genes from WGCNA modules identified in 3 month old TG-*Abi3-Gngt2*$^{-/-}$ mice. a. Genes within WGCNA modules associated with known KEGG pathways based on over-representation of enriched genes in TG-*Abi3-Gngt2*$^{-/-}$mice (relative to TG-*Abi3-Gngt2*$^{+/+}$) is depicted in a bubble plot. Pathways with an over-represented p-value ≤ 0.05, the number of module genes within the pathway >5 and an enrichment score >1.5 are depicted. The bubble plot is colored by p-value (blue color; higher p value is indicated by deeper blue hues) and sized by the enrichment score (circle diameter). b-e. WGCNA module membership is plotted against gene connectivity (kWithin) for genes identified within modules significantly correlated with *Abi3-Gngt2* genotype and related neuropathology traits in TG-*Abi3-Gngt2*$^{-/-}$mice. The top hub genes (as ranked by kWithin values) identified in each co-expression WGCNA modules of 3 month old TG-*Abi3-Gngt2*$^{-/-}$ mice relative to TG-*Abi3-Gngt2*$^{+/+}$ mice. The module members of honeydew1, plum3, sienna3 and plum4 modules are shown, with top hub genes tabulated. Module statistics are denoted by: kWithin, extent of gene connectivity within the module; MM, module membership value (of gene to module); GS, gene significance value to specific experimental trait. f. The overlap of genes within WGCNA modules with genes previously identified in AD-associated microglial and astrocytic sub-types signatures is expressed as odds ratio value. Higher odds ratio is indicated by warmer color. The different cell signatures are: neurotoxic A1 and neurotrophic A2 astrocyte [38]; Plaque-induced gene (PIG) network [21]; Disease-associated microglia (DAM), microglial neurodegenerative phenotype (MGnD) and homeostatic microglia [2425]. All *p* values are adjusted for multiple testing (padj). Higher odds ratio denotes higher correlation. Grey boxes indicate non-significant odds ratio values. 4 mice (2 male, 2 female) per cohort.

Additional file 11: Fig. S7. Somatic transgenesis modeling of tauopathy in *Abi3-Gngt2*$^{-/-}$ mice. a-c. *Abi3-Gngt2*$^{+/+}$ (WT) and *Abi3-Gngt2*$^{-/-}$ (KO) mice were injected with control vector (Control) or AAV expressing a double mutant (P301L/S320F) 0N/4R tau in the cerebral ventricles on neonatal day P0 and analyzed at 3 months of age. a. Representative images of ThioS-stained cortex of *Abi3-Gngt2*$^{+/+}$ or *Abi3-Gngt2*$^{-/-}$ mice injected with AAV-P301L/S320F tau or control vector shown. Three individual mice from each cohort are shown. b-c. Guanidine-insoluble brain lysates of AAV-P301L/S320F tau expressing *Abi3-Gngt2*$^{+/+}$ or *Abi3-Gngt2*$^{-/-}$ mice were separated on an immunoblot and probed with CP27 antibody (b) or CP13 antibody (c) to show presence of insoluble NFT tau. *N*=3 mice/condition. d-s. *Abi3-Gngt2*$^{+/+}$ and *Abi3-Gngt2*$^{-/-}$ mice were injected with control vector (Control) or AAV expressing human WT 0N/4R tau in the cerebral ventricles on neonatal day P0 and analyzed at 3 months (d-k) or 6 months (l-s) of age. Representative brain images of total human tau (detected with CP27 antibody, d, l), ptau (detected with CP13 antibody, f, n), astrocytes (detected with GFAP antibody, h, p) and microglia (detected with Iba-1 antibody, j, r) from cortex and hippocampus of *Abi3-Gngt2*$^{+/+}$ or *Abi3-Gngt2*$^{-/-}$ mice are shown. Quantitative analysis of antibody-stained brain sections (e, g, i, k, m, o, q, s) shown below corresponding stained brain images (d, f, h, j, l, n, p, r). Quantitative data in the graphs depicting the control vector cohort (*Abi3-Gngt2*$^{+/+}$ or *Abi3-Gngt2*$^{-/-}$ genotypes) is shared with corresponding data in Fig. 8 and Fig. 9 as these experiments were done simultaneously. For representative images of the control cohort, please refer to Fig. 8 and Fig. 9. Scale bar, 75 µm. *n*=4-6 mice/group. Data represents mean±sem. 1-way Anova; *****p*<0.0001; ****p*<0.001; ***p*<0.01; **p*<0.05.

Acknowledgements

We posthumously thank Dr. Peter Davies for anti tau antibodies.

The RNAseq results published here are in whole or in part based on data obtained from the AD Knowledge Portal (https://adknowledgeportal.org). The Mayo RNAseq study data was led by Dr. Nilüfer Ertekin-Taner (Mayo Clinic, Jacksonville, FL) as part of the multi-PI U01 AG046139 (MPIs Golde, Ertekin-Taner, Younkin, Price). Samples were provided from Mayo Clinic Brain Bank and Banner Sun Health Research Institute. Data collection was supported through funding by NIA grants P50 AG016574, R01 AG032990, U01 AG046139, R01 AG018023, U01 AG006576, U01 AG006786, R01 AG025711, R01 AG017216, R01 AG003949, NINDS grant R01 NS080820, CurePSP Foundation, and support from Mayo Foundation. Study data includes samples collected through the Sun Health Research Institute Brain and Body Donation Program of Sun City, Arizona. The Brain and Body Donation Program is supported by NINDS (U24 NS072026 National Brain and Tissue Resource for Parkinsons Disease and Related Disorders), NIA (P30 AG19610 Arizona Alzheimers Disease Core Center), the Arizona Department of Health Services (contract 211002, Arizona Alzheimers Research Center), the Arizona Biomedical Research Commission (contracts 4001, 0011, 05-901 and 1001 to the Arizona Parkinson's Disease Consortium), and the Michael J. Fox Foundation for Parkinsons Research.

Study data for the ROSMAP cohort was provided by the Rush Alzheimer's Disease Center and Rush University Medical Center, Chicago. Data collection was supported through funding by NIA grants P30AG10161 (ROS), R01AG15819 (ROSMAP; genomics and RNAseq), R01AG17917 (MAP), R01AG30146, R01AG36042 (5hC methylation, ATACseq), RC2AG036547 (H3K9Ac), R01AG36836 (RNAseq), R01AG48015 (monocyte RNAseq) RF1AG57473 (single-nucleus RNAseq), U01AG32984 (genomic and whole exome sequencing), U01AG46152 (ROSMAP AMP-AD, targeted proteomics), U01AG46161(TMT proteomics), U01AG61356 (whole genome sequencing, targeted proteomics, ROSMAP AMP-AD), the Illinois Department of Public Health (ROSMAP), and the Translational Genomics Research Institute (genomic). Additional phenotypic data can be requested at www.radc.rush.edu.

Authors' contributions

PC conceived the study and wrote the manuscript; KRI performed immunohistochemistry, ELISA and western blots and assembled final figures; KNM extracted RNA, performed RNAseq and analyzed data; JL, TEG, and SP performed in situ hybridization; MA, XW, ZQ, CF, TEG, and NET performed informatics analysis on human AMP-AD data; CBL performed in vitro

experiments; LZ, SS, and QV performed immunostaining and data analysis; EGDLC euthanized animals; PC maintained mouse colonies and performed neonatal injections; TEG and DR provided recombinant AAV. All authors read and reviewed the manuscript.

Funding
We thank the State of Florida Ed & Ethel Moore Alzheimer's Disease Research Program (8AZ16), NIH/NIA (U01 AG046139), University of Florida Neuromedicine Human Brain and Tissue Bank (funded in part by NIA P30AG066506), and McKnight Brain Institute for support.

Availability of data and materials
All data and materials will be available from the corresponding author upon publication on reasonable request.
The full RNAseq datasets presented in this manuscript has been deposited in AD Knowledge Portal (https://adknowledgeportal.org). The data can be accessed at https://www.synapse.org/ (Synapse ID:syn27312989). The AD Knowledge Portal is a platform for accessing data, analyses, and tools generated by the Accelerating Medicines Partnership (AMP-AD) Target Discovery Program and other National Institute on Aging (NIA)-supported programs to enable open-science practices and accelerate translational learning. The data, analyses and tools are shared early in the research cycle without a publication embargo on secondary use. Data is available for general research use according to the following requirements for data access and data attribution (https://adknowledgeportal.org/DataAccess/Instructions).

Declarations

Ethics approval and consent to participate
All animal experiments were done according to institutional guidelines.

Consent for publication
Not applicable.

Competing interests
The authors declare that they have no competing interests.

Author details
[1]Center for Translational Research in Neurodegenerative Disease, University of Florida, 1275 Center Drive, Gainesville, FL 32610, USA. [2]Department of Neurology, University of Florida, Gainesville, FL 32610, USA. [3]Department of Neuroscience, Mayo Clinic, Jacksonville, FL 32224, USA. [4]Department of Quantitative Health Sciences, Mayo Clinic, Jacksonville, FL 32224, USA. [5]Institute for Systems Biology, Seattle, WA 98109, USA. [6]Department of Neurology, Mayo Clinic, Jacksonville, FL 32224, USA. [7]Department of Pathology, University of Florida, Gainesville, FL 32610, USA. [8]McKnight Brain Institute, University of Florida, Gainesville, FL 32610, USA. [9]Department of Neuroscience, University of Florida, Gainesville, FL 32610, USA.

Received: 17 December 2021 Accepted: 6 July 2022
Published online: 27 July 2022

References

1. Jack CR Jr, et al. NIA-AA research framework: toward a biological definition of Alzheimer's disease. Alzheimers Dement. 2018;14(4):535–62.
2. Golde TE. Harnessing immunoproteostasis to treat neurodegenerative disorders. Neuron. 2019;101(6):1003–15.
3. Kinney JW, et al. Inflammation as a central mechanism in Alzheimer's disease. Alzheimers Dement (N Y). 2018;4:575–90.
4. Hansen DV, Hanson JE, Sheng M. Microglia in Alzheimer's disease. J Cell Biol. 2018;217(2):459–72.
5. Efthymiou AG, Goate AM. Late onset Alzheimer's disease genetics implicates microglial pathways in disease risk. Mol Neurodegener. 2017;12(1):43.
6. Sims R, et al. Rare coding variants in PLCG2, ABI3, and TREM2 implicate microglial-mediated innate immunity in Alzheimer's disease. Nat Genet. 2017;49(9):1373.
7. Conway OJ, et al. ABI3 and PLCG2 missense variants as risk factors for neurodegenerative diseases in Caucasians and African Americans. Mol Neurodegener. 2018;13(1):53.
8. Wightman DP, et al. A genome-wide association study with 1,126,563 individuals identifies new risk loci for Alzheimer's disease. Nat Genet. 2021;53(9):1276–82.
9. Miyazaki K, et al. Isolation and characterization of a novel human gene (NESH) which encodes a putative signaling molecule similar to e3B1 protein. Biochim Biophys Acta. 2000;1493(1–2):237–41.
10. Ichigotani Y, et al. Forced expression of NESH suppresses motility and metastatic dissemination of malignant cells. Cancer Res. 2002;62(8):2215–9.
11. Satoh JI, et al. Microglia express ABI3 in the brains of Alzheimer's disease and Nasu-Hakola disease. Intractable Rare Dis Res. 2017;6(4):262–8.
12. Yao Z, et al. A taxonomy of transcriptomic cell types across the isocortex and hippocampal formation. Cell. 2021;184(12):3222-3241 e26.
13. Bae J, et al. NESH regulates dendritic spine morphology and synapse formation. PLoS ONE. 2012;7(4):e34677.
14. Janus C, et al. A beta peptide immunization reduces behavioural impairment and plaques in a model of Alzheimer's disease. Nature. 2000;408(6815):979–82.
15. Chakrabarty P, et al. Capsid serotype and timing of injection determines AAV transduction in the neonatal mice brain. PLoS ONE. 2013;8(6):e67680.
16. Koller EJ, Gonzalez De La Cruz E, Machula T, Ibanez KR, Lin WL, Williams T, Riffe CJ, Ryu D, Strang KH, Liu X, Janus C, Golde TE, Dickson DW, Giasson BI, Chakrabarty P. Combining P301L and S320F tau variants produces a novel accelerated model of tauopathy. Hum Mol Genet. 2019;28(19):3255.
17. Dobin A, et al. STAR: ultrafast universal RNA-seq aligner. Bioinformatics. 2013;29(1):15–21.
18. Lawrence M, et al. Software for computing and annotating genomic ranges. PLoS Comput Biol. 2013;9(8):e1003118.
19. Love MI, Huber W, Anders S. Moderated estimation of fold change and dispersion for RNA-seq data with DESeq2. Genome Biol. 2014;15(12):550.
20. Zhang Y, et al. An RNA-sequencing transcriptome and splicing database of glia, neurons, and vascular cells of the cerebral cortex. J Neurosci. 2014;34(36):11929–47.
21 Chen WT, et al. Spatial transcriptomics and in situ sequencing to study Alzheimer's disease. Cell. 2020;182(4):976-991 e19.
22. Friedman BA, et al. Diverse brain myeloid expression profiles reveal distinct microglial activation states and aspects of Alzheimer's disease not evident in mouse models. Cell Rep. 2018;22(3):832–47.
23 Hammond TR, et al. Single-cell RNA sequencing of microglia throughout the mouse lifespan and in the injured brain reveals complex cell-state changes. Immunity. 2019;50(1):253-271 e6.
24. Keren-Shaul H, et al. A unique microglia type associated with restricting development of Alzheimer's disease. Cell. 2017;169(7):1276-1290 e17.
25. Krasemann S, et al. The TREM2-APOE pathway drives the transcriptional phenotype of dysfunctional microglia in neurodegenerative diseases. Immunity. 2017;47(3):566-581 e9.
26 Sala Frigerio C, et al. The major risk factors for Alzheimer's disease: age, sex, and genes modulate the microglia response to abeta plaques. Cell Rep. 2019;27(4):1293-1306 e6.
27. Langfelder P, Horvath S. WGCNA: an R package for weighted correlation network analysis. BMC Bioinformatics. 2008;9:559.
28 Langfelder P, Horvath S. Fast R functions for robust correlations and hierarchical clustering. J Stat Softw. 2012;46(11):i11.
29. Young MD, et al. Gene ontology analysis for RNA-seq: accounting for selection bias. Genome Biol. 2010;11(2):R14.
30 Dejanovic B, et al. Changes in the synaptic proteome in tauopathy and rescue of Tau-induced synapse loss by C1q antibodies. Neuron. 2018;100(6):1322-1336 e7.
31. Allen M, et al. Gene expression, methylation and neuropathology correlations at progressive supranuclear palsy risk loci. Acta Neuropathol. 2016;132(2):197.
32. De Jager PL, et al. A multi-omic atlas of the human frontal cortex for aging and Alzheimer's disease research. Sci Data. 2018;5:180142.
33. Wan YW, et al. Meta-analysis of the Alzheimer's disease human brain transcriptome and functional dissection in mouse models. Cell Rep. 2020;32(2):107908.

34. Al-Ouran R, et al. A portal to visualize transcriptome profiles in mouse models of neurological disorders. Genes (Basel). 2019;10(10):759.
35. Walker DG. Defining activation states of microglia in human brain tissue: an unresolved issue for Alzheimer's disease. Neuroimmunol Neuroinflamm. 2020;7:194–214.
36. Liu CY, et al. Emerging roles of astrocytes in neuro-vascular unit and the tripartite synapse with emphasis on reactive gliosis in the context of Alzheimer's disease. Front Cell Neurosci. 2018;12:193.
37. Mendoza MC. Phosphoregulation of the WAVE regulatory complex and signal integration. Semin Cell Dev Biol. 2013;24(4):272–9.
38. Liddelow SA, et al. Neurotoxic reactive astrocytes are induced by activated microglia. Nature. 2017;541(7638):481–7.
39. Llorens F, et al. YKL-40 in the brain and cerebrospinal fluid of neurodegenerative dementias. Mol Neurodegener. 2017;12(1):83.
40. Zhou Y, et al. Human and mouse single-nucleus transcriptomics reveal TREM2-dependent and TREM2-independent cellular responses in Alzheimer's disease. Nat Med. 2020;26(1):131–42.
41. Zhang B, et al. Integrated systems approach identifies genetic nodes and networks in late-onset Alzheimer's disease. Cell. 2013;153(3):707–20.
42. Patir A, et al. A core transcriptional signature of human microglia: derivation and utility in describing region-dependent alterations associated with Alzheimer's disease. Glia. 2019;67(7):1240–53.
43. Beckman D, et al. A novel tau-based rhesus monkey model of Alzheimer's pathogenesis. Alzheimers Dement. 2021;17(6):933–45.
44. Sekino S, et al. The NESH/Abi-3-based WAVE2 complex is functionally distinct from the Abi-1-based WAVE2 complex. Cell Commun Signal. 2015;13:41.
45. Huang CH, et al. The involvement of Abl and PTP61F in the regulation of Abi protein localization and stability and lamella formation in Drosophila S2 cells. J Biol Chem. 2007;282(44):32442–52.
46. Simonazzi E, et al. Abi3 regulates microglial ramification and dynamic tissue surveillance in vivo. bioRxiv. 2021. https://www.biorxiv.org/content/10.1101/2021.03.19.436147v1
47. Karahan H, et al. Deletion of Abi3 gene locus exacerbates neuropathological features of Alzheimer's disease in a mouse model of Abeta amyloidosis. Sci Adv. 2021;7(45):eabe3954.
48. Bemiller SM, et al. TREM2 deficiency exacerbates tau pathology through dysregulated kinase signaling in a mouse model of tauopathy. Mol Neurodegener. 2017;12(1):74.
49. Sayed FA, et al. Differential effects of partial and complete loss of TREM2 on microglial injury response and tauopathy. Proc Natl Acad Sci U S A. 2018;115(40):10172–7.
50. Leyns CEG, et al. TREM2 deficiency attenuates neuroinflammation and protects against neurodegeneration in a mouse model of tauopathy. Proc Natl Acad Sci U S A. 2017;114(43):11524–9.
51 Lee SH, et al. Trem2 restrains the enhancement of tau accumulation and neurodegeneration by beta-amyloid pathology. Neuron. 2021;109(8):1283-1301 e6.
52. Burberry A, et al. C9orf72 suppresses systemic and neural inflammation induced by gut bacteria. Nature. 2020;582(7810):89–94.
53. Erny D, et al. Host microbiota constantly control maturation and function of microglia in the CNS. Nat Neurosci. 2015;18(7):965–77.
54. Ong OC, et al. Gene structure and chromosome localization of the G gamma c subunit of human cone G-protein (GNGT2). Genomics. 1997;44(1):101–9.
55. Audrain M, et al. Integrative approach to sporadic Alzheimer's disease: deficiency of TYROBP in a tauopathy mouse model reduces C1q and normalizes clinical phenotype while increasing spread and state of phosphorylation of tau. Mol Psychiatry. 2019;24(9):1383–97.
56. Haure-Mirande JV, et al. Integrative approach to sporadic Alzheimer's disease: deficiency of TYROBP in cerebral Abeta amyloidosis mouse normalizes clinical phenotype and complement subnetwork molecular pathology without reducing Abeta burden. Mol Psychiatry. 2019;24(3):431–46.
57. Meilandt WJ, et al. Trem2 deletion reduces late-stage amyloid plaque accumulation, elevates the Abeta42:Abeta40 Ratio, and exacerbates axonal dystrophy and dendritic spine loss in the PS2APP Alzheimer's mouse model. J Neurosci. 2020;40(9):1956–74.
58. Parhizkar S, et al. Loss of TREM2 function increases amyloid seeding but reduces plaque-associated ApoE. Nat Neurosci. 2019;22(2):191–204.
59. Jay TR, et al. TREM2 deficiency eliminates TREM2+ inflammatory macrophages and ameliorates pathology in Alzheimer's disease mouse models. J Exp Med. 2015;212(3):287–95.
60. Chakrabarty P, et al. IFN-gamma promotes complement expression and attenuates amyloid plaque deposition in amyloid beta precursor protein transgenic mice. J Immunol. 2010;184(9):5333–43.
61. Li A, et al. IFN-gamma promotes tau phosphorylation without affecting mature tangles. FASEB J. 2015;29(10):4384–98.
62. Shaftel SS, et al. Sustained hippocampal IL-1 beta overexpression mediates chronic neuroinflammation and ameliorates Alzheimer plaque pathology. J Clin Invest. 2007;117(6):1595–604.
63. Ghosh S, et al. Sustained interleukin-1beta overexpression exacerbates tau pathology despite reduced amyloid burden in an Alzheimer's mouse model. J Neurosci. 2013;33(11):5053–64.
64. Lee H, et al. Cell type-specific transcriptomics reveals that mutant huntingtin leads to mitochondrial rna release and neuronal innate immune activation. Neuron. 2020;107(5):891-908 e8.
65. Bhaskar K, et al. Regulation of tau pathology by the microglial fractalkine receptor. Neuron. 2010;68(1):19–31.
66. Lee S, et al. CX3CR1 deficiency alters microglial activation and reduces beta-amyloid deposition in two Alzheimer's disease mouse models. Am J Pathol. 2010;177(5):2549–62.
67. Hamelin L, et al. Early and protective microglial activation in Alzheimer's disease: a prospective study using 18F-DPA-714 PET imaging. Brain. 2016;139(Pt 4):1252–64.
68. Fan Z, et al. An early and late peak in microglial activation in Alzheimer's disease trajectory. Brain. 2017;140(3):792–803.
69. Patel AG, et al. Innate immunity stimulation via CpG oligodeoxynucleotides ameliorates Alzheimer's disease pathology in aged squirrel monkeys. Brain. 2021;144(7):2146–65.
70. Boros BD, et al. Dendritic spines provide cognitive resilience against Alzheimer's disease. Ann Neurol. 2017;82(4):602–14.
71. Chakrabarty P, et al. Massive gliosis induced by interleukin-6 suppresses Abeta deposition in vivo: evidence against inflammation as a driving force for amyloid deposition. FASEB J. 2010;24(2):548–59.
72. Nisbet RM, et al. Tau aggregation and its interplay with amyloid-beta. Acta Neuropathol. 2015;129(2):207–20.
73. Siddiqui TA, et al. Regulation of podosome formation, microglial migration and invasion by Ca(2+)-signaling molecules expressed in podosomes. J Neuroinflammation. 2012;9:250.
74. Craig-Schapiro R, et al. YKL-40: a novel prognostic fluid biomarker for preclinical Alzheimer's disease. Biol Psychiatry. 2010;68(10):903–12.
75. Lananna BV, et al. Chi3l1/YKL-40 is controlled by the astrocyte circadian clock and regulates neuroinflammation and Alzheimer's disease pathogenesis. Sci Transl Med. 2020;12(574):eaax3519.
76. Magno L, et al. Alzheimer's disease phospholipase C-gamma-2 (PLCG2) protective variant is a functional hypermorph. Alzheimers Res Ther. 2019;11(1):16.
77. Liu Y, Beyer A, Aebersold R. On the dependency of cellular protein levels on mRNA abundance. Cell. 2016;165(3):535–50.
78. Bae J, et al. F-actin-dependent regulation of NESH dynamics in rat hippocampal neurons. PLoS ONE. 2012;7(4):e34514.
79 Griciuc A, et al. TREM2 acts downstream of CD33 in modulating microglial pathology in Alzheimer's disease. Neuron. 2019;103(5):820-835 e7.
80. Courtney KD, et al. Localization and phosphorylation of Abl-interactor proteins, Abi-1 and Abi-2, in the developing nervous system. Mol Cell Neurosci. 2000;16(3):244–57.

Publisher's Note